

- 1
- 2
- 3
- 4
- 5
- 6
- 7
- 8
- 9
- 10
- 11
- 12
- 13
- 14
- 15
- 16
- 17
- 18
- 19
- 20
- 21
- 22
- 23
- 24
- 25
- 26
- 27
- 28

- 1
- 2
- 3
- 4
- 5
- 6
- 7
- 8
- 9
- 10
- 11
- 12
- 13
- 14
- 15
- 16
- 17
- 18
- 19
- 20
- 21
- 22
- 23
- 24
- 25
- 26
- 27
- 28

- 1
- 2
- 3
- 4
- 5
- 6
- 7
- 8
- 9
- 10
- 11
- 12
- 13
- 14
- 15
- 16
- 17
- 18
- 19
- 20
- 21
- 22
- 23
- 24
- 25
- 26
- 27
- 28

- 1
- 2
- 3
- 4
- 5
- 6
- 7
- 8
- 9
- 10
- 11
- 12
- 13
- 14
- 15
- 16
- 17
- 18
- 19
- 20
- 21
- 22
- 23
- 24
- 25
- 26
- 27
- 28

- 1
- 2
- 3
- 4
- 5
- 6
- 7
- 8
- 9
- 10
- 11
- 12
- 13
- 14
- 15
- 16
- 17
- 18
- 19
- 20
- 21
- 22
- 23
- 24
- 25
- 26
- 27
- 28

- 1
- 2
- 3
- 4
- 5
- 6
- 7
- 8
- 9
- 10
- 11
- 12
- 13
- 14
- 15
- 16
- 17
- 18
- 19
- 20
- 21
- 22
- 23
- 24
- 25
- 26
- 27
- 28

- 1
- 2
- 3
- 4
- 5
- 6
- 7
- 8
- 9
- 10
- 11
- 12
- 13
- 14
- 15
- 16
- 17
- 18
- 19
- 20
- 21
- 22
- 23
- 24
- 25
- 26
- 27
- 28

- 1
- 2
- 3
- 4
- 5
- 6
- 7
- 8
- 9
- 10
- 11
- 12
- 13
- 14
- 15
- 16
- 17
- 18
- 19
- 20
- 21
- 22
- 23
- 24
- 25
- 26
- 27
- 28

- 1
- 2
- 3
- 4
- 5
- 6
- 7
- 8
- 9
- 10
- 11
- 12
- 13
- 14
- 15
- 16
- 17
- 18
- 19
- 20
- 21
- 22
- 23
- 24
- 25
- 26
- 27
- 28

- 1
- 2
- 3
- 4
- 5
- 6
- 7
- 8
- 9
- 10
- 11
- 12
- 13
- 14
- 15
- 16
- 17
- 18
- 19
- 20
- 21
- 22
- 23
- 24
- 25
- 26
- 27
- 28

## ABSTRACT

A new version of the atmosphere-ocean general circulation model cooperatively developed in the Japanese research community, known as the Model for Interdisciplinary Research on Climate (MIROC), was developed. A century-long control experiment was performed using the new version (MIROC5) with the standard resolution of the T85 atmosphere and 1° ocean models. The climatological mean state and variability are then compared with observations and those in a previous version (MIROC3) with two different resolutions, coarser and finer than the resolution of MIROC5.

A few aspects of the mean field in MIROC5 are similar to or slightly worse than MIROC3, but otherwise the climatological features are considerably better. In particular, improvements are found in precipitation, zonal-mean atmospheric fields, equatorial ocean subsurface fields, and the simulation of El Niño-Southern Oscillation. The difference between MIROC5 and the previous model is larger than that between the two MIROC3 runs, indicating a greater impact of updating parameterization schemes on the model climate than increasing the model resolution. The mean cloud property obtained from the sophisticated prognostic schemes in MIROC5 shows good agreement with satellite measurements. MIROC5 reveals an equilibrium climate sensitivity of 2.6 K, which is lower than that in MIROC3 by 1 K. This is probably due to the negative feedback of low clouds to the increasing concentration of CO<sub>2</sub>, which is opposite to that in MIROC3.

## 53    **1. Introduction**

54            A comprehensive climate model that couples the atmosphere and ocean general  
55    circulation models together with the land and sea ice modules is called the coupled  
56    general circulation model (CGCM), or the global climate model. The development of  
57    CGCMs has a history of several decades, and they provide a unique way of physically-  
58    based modeling the global climate and its variability (cf. Meehl et al. 2007; Reichler and  
59    Kim 2008). As human-induced climate change has attracted wider societal attention,  
60    CGCMs have become more important tools than ever (IPCC 2007).

61            Despite the usefulness of CGCMs, it is well known that such models still  
62    contain errors in various fields such as precipitation and sea surface temperature (SST),  
63    and reveal considerable disagreement, for example, in the cloud feedback when  
64    performing climate change simulations (e.g., Bony and Dufresne 2005). Some aspects  
65    of the model errors can certainly be reduced by increasing the resolution for either the  
66    atmosphere or ocean component (e.g., Shaffrey et al. 2009). High-resolution atmosphere  
67    models produce an improved precipitation distribution arising from higher-resolution  
68    orography (Pope and Stratton 2002; Jung et al. 2006; Gent et al. 2009) and more  
69    realistic tropical cyclone frequency (Oouchi et al. 2006). Similarly, the SST and ocean  
70    surface fields are better simulated by partly resolving oceanic eddies (Semtner and  
71    Chervin 1992; Sakamoto et al. 2004). However, other errors attributed to complicated  
72    feedback processes are not necessarily reduced by increasing the resolution without  
73    changing the parameterization schemes. In this regard, not only the use of higher  
74    resolution models but also continuously developing the model itself is clearly a key  
75    issue for better reproducing the past climate variability, projecting future climate change,  
76    and understanding their mechanisms.

77           In this paper, we present the basic results obtained from a new version of our  
78 coupled model, the Model for Interdisciplinary Research on Climate (MIROC),  
79 developed jointly at the Center for Climate System Research (CCSR), University of  
80 Tokyo, National Institute for Environmental Studies (NIES), and Japan Agency for  
81 Marine-Earth Science and Technology. This new version, called MIROC5, will be used  
82 for the forthcoming Intergovernmental Panel on Climate Change (IPCC) Fifth  
83 Assessment Report (AR5). The previous version, MIROC3 (K-1 model developers  
84 2004), included a standard physics package and was well tuned at the time of the Fourth  
85 Assessment Report (AR4). The model showed mean states that were relatively close to  
86 the average of CGCMs participated in the Coupled Model Intercomparison Phase 3  
87 (CMIP3). There were, however, deficiencies in the natural variability and climate  
88 sensitivity (see Santer et al. 2009 for example). One important shortcoming was the  
89 extremely weak El Niño-Southern Oscillation (ENSO) even though the equatorial mean  
90 states were good (Guilyardi et al. 2009a). In addition, the cloud representation in  
91 MIROC3 was crude; the prognostic variable was the total water mixing ratio, from  
92 which the cloud fraction was diagnosed by using a conventional large-scale  
93 condensation (LSC) scheme, and the water/ice separation was accomplished simply by  
94 referring to temperature. It has been reported that the climate sensitivity heavily  
95 depends on the response of mixed-phase clouds to radiative forcing (Tsushima et al.  
96 2006), so the cloud representation had to be totally reconsidered.

97           As will be described in the next section, most parts of the model, except for the  
98 atmospheric dynamical core, were updated or even replaced with new parameterization  
99 schemes in MIROC5. A century-long, pre-industrial simulation was performed with the  
100 standard resolution of T85L40 atmosphere and approximately 1° ocean component

101 models. The atmospheric resolution is between the two MIROC3 products included in  
102 AR4, i.e., “MIROC3med” and “MIROC3hi”, which adopted the T42L20 and T106L56  
103 atmosphere components, respectively. The horizontal resolution for the ocean  
104 components in MIROC5 is the same as that used in MIROC3med, and coarser than that  
105 of MIROC5hi, which used an eddy-permitting ocean model with a  $1/4^\circ$  by  $1/6^\circ$   
106 resolution. A comparison of the climatology between MIROC5 and the two data sets  
107 from the MIROC3 runs enables us to evaluate the impact of the new model  
108 configuration relative to the effect of increasing the model resolution. Overall, the new  
109 standard resolution is close to that of MIROC3med, but it is demonstrated that the  
110 difference between the two model versions is greater than that between MIROC3med  
111 and MIROC3hi. It may have been better to run MIROC5 with the same resolution as  
112 MIROC3 to thoroughly investigate the resolution vs. parameterization issue, but the  
113 standard resolution of MIROC5 was chosen mainly due to the limitation of  
114 computational resources.

115       This paper is organized as follows. In the next section, the framework of  
116 MIROC5 is described without the details of the individual parameterization schemes,  
117 which have been presented elsewhere. In section 3, the time-mean states and interannual  
118 variability are compared with observations and those obtained from MIROC3. The  
119 results demonstrate that the deficiency observed in MIROC3 is greatly reduced in  
120 several respects. The investigation of model behavior, by an abrupt quadrupling  $\text{CO}_2$   
121 ( $\text{CO}_2 \times 4$ ) experiment, is described in section 4. The climate sensitivity of MIROC5 is  
122 then briefly examined and is found to be lower than that of the previous model version.  
123 Section 5 presents the concluding discussion.

124

## 125    **2. Model description**

126            As described by K-1 developers (2004), MIROC3 couples the following  
127    component models. The atmosphere model is the CCSR/NIES/FRCGC AGCM  
128    (Numaguti et al. 1997), which is based on a global spectral dynamical core and includes  
129    a standard physics package. The ocean model is the CCSR Ocean COmponent model  
130    (COCO, Hasumi 2006), which includes a sea ice model. A land model that includes a  
131    river module is also coupled. MIROC5 was developed based on MIROC3, but many of  
132    the schemes have been replaced as follows.

133

### 134    *a. Atmosphere component*

#### 135    1) Dynamical core

136            In recent years, atmospheric dynamical cores tend to be represented either by  
137    finite volume or finite difference schemes that are favorable for high-resolution  
138    computing (e.g., Tomita and Satoh 2004, Lin 2004). In this regard, the spectral  
139    dynamical core that we use in MIROC5, as in the previous version, may be outdated,  
140    and will be replaced in the next stage.

141            We used the vertical  $\sigma$  coordinate in MIROC3, in which the model top was  
142    about 8 hPa in the medium resolution. In MIROC5, we adopt a hybrid  $\sigma$ -p coordinate  
143    (cf. Arakawa and Konor 1996), which is shared by our Earth system model (ESM), with  
144    the model top at around 0.003 hPa (Watanabe et al. 2008). The standard vertical  
145    resolution of the MIROC5 atmosphere is 40 levels up to 3 hPa. This resolution is  
146    between MIROC3med and MIROC3hi, which had 20 and 56  $\sigma$  levels, respectively. The  
147    Asselin time filter has also been modified following Williams' method (2009).

148

149 2) Radiation

150 The radiative transfer in MIROC5 is calculated by an updated version of the  $k$ -  
151 distribution scheme used in MIROC3 (Sekiguchi and Nakajima 2008). This scheme  
152 results in improvements in the line absorption and continuum absorption, with an  
153 increase in the number of absorption bands from 18 to 29. These changes all contribute  
154 to a more accurate calculation of radiative heating and reduce a cold bias near the  
155 tropopause, which was found in MIROC3 (cf. section 3b).

156

157 3) Cumulus convection

158 The cumulus scheme employed in MIROC5 is one that was recently developed  
159 by Chikira and Sugiyama (2009). It is an entraining-plume model, where the lateral  
160 entrainment rate varies vertically depending on the surrounding environment. Its  
161 formulation is similar to the scheme by Gregory (2001), who assumed that a certain  
162 fraction of buoyancy-generated energy is consumed by the entrainment process.  
163 Multiple cloud types having different cloud tops are considered, as done by Arakawa  
164 and Schubert (1974), except for the representation according to the updraft velocity at  
165 the cloud base. The cloud base mass flux is determined with a prognostic convective  
166 kinetic energy closure (Xu 1993; Pan and Randall 1998), which has been employed in  
167 MIROC3.

168 The sensitivity of the scheme to temperature and humidity profiles and the  
169 scheme's impact on model climatology have been documented by Chikira and  
170 Sugiyama (2009) and Chikira (2009). The scheme tends to produce larger entrainment  
171 rate near the cloud base as compared with Pan and Randall's scheme. By incorporating  
172 the state-dependent entrainment rate, deep convection tends to be effectively suppressed

173 when the environment is dry in the free troposphere. This enables us to eliminate an  
174 artificial triggering function for the deep convection, which was used in the previous  
175 version (Emori et al. 2005).

176

#### 177 4) Cloud and cloud microphysics

178 In MIROC3, the formation and dissipation of clouds were represented by a  
179 diagnostic LSC scheme proposed by Le Treut and Li (1991) and a simple microphysics  
180 scheme. Ogura et al. (2008) found that the climate sensitivity in MIROC3 is primarily  
181 controlled by the crude representation of clouds, and hence, may not be realistic.

182 In order to better represent cloud and cloud-radiative feedback, we made two  
183 major changes in MIROC5: the development of a prognostic LSC scheme (Watanabe et  
184 al. 2009) and the implementation of a bulk microphysical scheme (Wilson and Ballard  
185 1999). The new LSC scheme solves prognostic equations for the subgrid scale variance  
186 and skewness of a conservative quantity associated with temperature and total water,  
187 and hence, represents various cloud regimes having different optical properties. The  
188 cloud microphysical scheme explicitly deals with the warm and cold rain processes:  
189 nucleation, deposition and sublimation, riming, ice melting and rain drops capturing by  
190 falling ice, etc.

191 Because the original scheme by Watanabe et al. (2009) did not consider the  
192 cloud ice, we modified the scheme when coupling it with the Wilson and Ballard's  
193 (1999) scheme. Since the LSC scheme employs a "fast condensation" assumption that is  
194 not relevant to ice, the ice mixing ratio is conserved in the LSC process by assuming  
195 that the cloud ice exists preferentially in a subgrid area having the largest amount of  
196 total condensate. Specifically, the mixed phase cloud is generated when the condensate



197 amount is more than the ice content, whereas the cloud fraction and vapor amount are  
198 adjusted in the case of a pure ice cloud when the condensate amount is less than the ice  
199 content. By combining the two schemes, the fraction of cloud liquid and ice is no longer  
200 just a simple function of temperature, and the processes controlling climate sensitivity  
201 will also be qualitatively different from those in the previous version (cf. section 4).

202

## 203 5) Turbulence

204 The vertical diffusion scheme is based on Nakanishi and Niino (2001, 2004). It  
205 is a Mellor-Yamada (1974, 1982) type scheme with a closure level of 2.5, but improved  
206 in several respects. The master length scale,  $L$ , is newly devised for large-scale models  
207 and determined by the harmonic mean of three length scales,  $L_S$ ,  $L_T$ , and  $L_B$ , which  
208 characterize the surface layer, convective boundary layer, and stably stratified layer,  
209 respectively. Shear and buoyancy effects on the pressure covariance terms have been  
210 added, and the closure constants were reevaluated by large eddy simulation outputs (cf.  
211 Nakanishi and Niino 2001, 2004). The effect of the vapor-liquid transition on buoyancy  
212 is considered by using the new LSC scheme. The improved turbulence scheme reduces  
213 some common deficiencies of the Mellor-Yamada scheme (cf. section 3b).

214 The formulation of  $L$  in the original scheme was not necessarily adequate for  
215 the free atmosphere when its stability was reduced by radiative cooling due to clouds.  
216 Therefore, the master length scale of the free atmosphere is given by the harmonic mean  
217 of  $L_S$ ,  $L_A$ , and  $L_{\max}$ , where  $L_A$ , expressed in terms of the turbulence kinetic energy  
218 (TKE) and the Brunt-Väisälä frequency, represents a length scale on which an air parcel  
219 with a given TKE can be vertically displaced in a stably stratified layer. A constant of  
220  $L_{\max} = 500$  m gives the upper limit.

221

## 222 6) Aerosols

223 An aerosol module in MIROC, called SPRINTARS, predicts the mass mixing  
224 ratios of the main tropospheric aerosols: carbonaceous (black carbon and organic  
225 matter), sulfate, soil dust, and sea salt, as well as the precursor gases of sulfate, i.e.,  
226 sulfur dioxide and dimethylsulfide (DMS). The aerosol transport processes include  
227 emission, advection, diffusion, sulfur chemistry, wet deposition, dry deposition, and  
228 gravitational settling. The emissions of soil dust, sea salt, and DMS are calculated using  
229 the internal parameters of the model, and external emission inventories are used for the  
230 other aerosol sources.

231 SPRINTARS is coupled with the radiation and cloud microphysics schemes to  
232 calculate the direct and indirect effects of the aerosols. In the calculation of the direct  
233 effect, the refractive indices depending on wavelengths, size distributions, and  
234 hygroscopic growth are considered for each kind of aerosol. The aerosol semi-direct  
235 effect is also included as a consequence of the combination of the aerosol module and  
236 other schemes. A prognostic scheme for determining the cloud droplet and ice crystal  
237 number concentrations is introduced for calculating the aerosol indirect effect and cloud  
238 nucleation process. Changes in their radii and precipitation rates due to the indirect  
239 effect impact the radiation and cloud processes. Readers may refer to Takemura et al.  
240 (2005, 2009, references therein) for further details on the present version of  
241 SPRINTARS.

242

### 243 ***b. Ocean component***

#### 244 1) General features

245           The ocean general circulation model used for MIROC5 is COCO version 4.5.  
246   The primary update from the previous version includes a change in the coordinate  
247   system. The governing equations in COCO4.5 are formulated on a generalized  
248   curvilinear horizontal coordinate. The generalization is made by transforming the  
249   longitude-latitude coordinate system and its meridians and latitude circles using the  
250   polar stereographic projection and conformal mapping, following Bestsen et al. (1999).  
251   The North Pole (South Pole) of the model coordinate system is moved to 40°W, 80°N  
252   over Greenland (40°W, 80°S over Antarctica). The zonal resolution is a fixed 1.4°  
253   whereas the meridional resolution is 0.5° at latitudes equatorward of 8°, 1.4° at higher  
254   latitudes (poleward of 65°), with a smooth transition in between (256 by 224 grids for  
255   zonal and meridional direction). This horizontal resolution is approximately the same as  
256   the ocean model in MIROC3med, but the number of vertical levels has been increased  
257   from 43 to 49, excluding the bottom boundary layer. The vertical grid spacing varies  
258   with depth: 2.5 m at the surface, 20 m at the depth of 100 m, 100 m at the depth of 1000  
259   m, and 250 m below the 2000 m depth. The other features of the discretization follow  
260   the previous version (cf. Hasumi 2006 and also at [http://www.ccsr.u-](http://www.ccsr.u-tokyo.ac.jp/~hasumi/COCO/)  
261   tokyo.ac.jp/~hasumi/COCO/).

262           In the model bathymetry, the Bering Strait is represented by a two-grid gap, so  
263   that there is only one velocity grid point at the strait. The water pathway through the  
264   Canadian Archipelago is also represented by artificially excavating a channel. The  
265   Mediterranean Sea is represented as an isolated basin. At the strait of Gibraltar, the sea  
266   surface elevation and tracers are artificially exchanged by two-way linear damping with  
267   the time constants of 100 and 300 days, respectively, at depths above 1260 m (30<sup>th</sup>  
268   level).

269 The numerical scheme for the tracer advection is replaced by a second-order  
270 moment method (Prather 1986). The vertical mixing of momentum and tracers uses a  
271 harmonic formulation. In order to eliminate checker-board noise in the sea surface  
272 elevation field, we apply a weak horizontal diffusion with a coefficient of  $50 \text{ m}^2 \text{ s}^{-1}$ ,  
273 which does not violate the conservation of tracer quantities.

274

## 275 2) Physical parameterization

276 Some of the physical parameterization schemes employed in COCO4.5 have  
277 been updated. The treatment of the vertical convection, bottom boundary layer,  
278 background diffusivity, and penetration of shortwave radiation remains unchanged (see  
279 Hasumi 2006 for the references). To reproduce the formation of North Pacific  
280 intermediate water (Tally 1993; Yasuda 1997), the background diffusivity is raised to  
281  $2.0 \times 10^{-2} \text{ m}^2 \text{ s}^{-1}$  below the 100 m depth along the Kuril Islands (from the tip of the  
282 Kamchatka Peninsula to Hokkaido), as suggested by a direct calculation of tidal effects  
283 (Nakamura et al. 2000).

284 The turbulent mixing process is represented by the parameterization of Noh and  
285 Kim (1999), as in the previous version. However, the definition of the turbulent Prandtl  
286 number has been modified following Noh et al. (2005). The lateral mixing process as  
287 represented by harmonic viscosity has also been revised. Its coefficient is  
288  $3.0 \times 10^4 \Delta x / \Delta x_{\text{max}} \text{ m}^2 \text{ s}^{-1}$ , where  $\Delta x$  and  $\Delta x_{\text{max}}$  are the local and maximum longitudinal  
289 grid intervals, respectively, and it is reduced to  $2.0 \times 10^4 \Delta x / \Delta x_{\text{max}} \text{ m}^2 \text{ s}^{-1}$  at the equator,  
290 with a Gaussian distribution between  $15^\circ\text{S}$  and  $15^\circ\text{N}$  to reproduce a realistic equatorial  
291 undercurrent (EUC), as suggested by Large et al. (2001). The harmonic horizontal  
292 diffusion, isopycnal diffusion, and horizontal diffusion of the isopycnal layer thickness

293 (Gent et al. 1995) are also applied with coefficients of  $1.0 \times 10^2$ ,  $1.0 \times 10^3$ , and  
294  $3.0 \times 10^2 \text{ m}^2 \text{ s}^{-1}$ , respectively.

295 The bottom boundary layer is applied at high latitudes to the north of  $49^\circ\text{N}$  and  
296 to the south of  $56^\circ\text{S}$  following Nakano and Suginohara (2002). The Rayleigh drag  
297 coefficient is taken to be the same as the Coriolis parameter above 2000 m for the  
298 Northern Hemisphere (NH) and above 4000 m for the Southern Hemisphere (SH), with  
299 a value of zero below, as suggested by Nakano and Suginohara (2002).

300

### 301 *c. Sea ice component*

302 In MIROC3, the sea ice is treated as a two-dimensional continuum in terms of  
303 dynamics, with which the concentration, thickness, and horizontal velocity components  
304 are predicted at each grid. In MIROC5, we introduce a multi-category in that the sea ice  
305 concentration, ice thickness, snow thickness, and energy of ice melting are predicted for  
306 multiple categories in a grid cell. The sea ice model calculates the evolution of the  
307 subgrid scale sea ice thickness distribution following the governing equation by  
308 Thorndike et al. (1975). The thickness distribution and evaluation of the mechanical  
309 redistribution term are discretized according to Bitz et al. (2001). The sea ice at each  
310 horizontal grid is divided into five categories, plus open water. The lower bounds of the  
311 ice thickness for these categories are 0.3, 0.6, 1, 2.5, and 5 m.

312

#### 313 1) Thermodynamics

314 The heat capacity of sea ice is considered in the new sea ice module. The growth,  
315 melting, and temperature change of sea ice are computed based on the energy-  
316 conserving thermodynamic scheme of Bitz and Lipscomb (1999). We use this scheme

317 with only one layer for sea ice. The temperature of snow is not considered since snow is  
318 assumed to have no heat capacity. The salinity of sea ice is fixed at 5 psu. The  
319 penetration of solar radiation into the snow or ice is not taken into account. The albedo  
320 values for a bare ice surface are fixed at 0.8 and 0.65 for the visible and near-infrared  
321 bands, respectively. The surface albedo over a snow-covered area depends on  
322 temperature by taking into consideration the existence of partial snow cover at a  
323 relatively high temperature. It is 0.9 (0.8) for a temperature lower than -5 °C, 0.8 (0.65)  
324 at 0 °C, and changes linearly in between for the visible (near-infrared) radiation.

325 In open water, including that of a partially ice-covered grid, cooling forms new  
326 ice if the sea water temperature is at the freezing point. The newly formed ice is added  
327 to the thinnest category with the same thickness when it already exists. The new ice  
328 thickness is otherwise equal to the lower limit (i.e., 0.3 m). On the other hand, the  
329 warming of open water melts the sea ice. This occurs from the bottom of the sea ice.

330 Once the thermodynamic growth rates for each category are determined, the  
331 linear remapping scheme of Lipscomb (2001) is applied. It evaluates the  
332 thermodynamic transfer of the ice between categories by assuming a linear ice thickness  
333 distribution within the categories.

334

## 335 2) Dynamics

336 In the multi-category sea ice model, thermodynamic variables such as the sea ice  
337 concentration for each category are advected by the prognostic ice velocity, which is  
338 common for all the categories in a grid. A simple first-order upstream scheme is  
339 employed for computing the advection term. The dynamical schemes are otherwise the  
340 same as the previous version, except for changes in the parameter values: the strength of

341 the ice per unit thickness and concentration is set at  $2.0 \times 10^2 \text{ N m}^{-1}$ , and the ice-ocean  
342 drag coefficient has been increased to 0.02.

343

#### 344 *d. Land component*

345 MIROC5 adopts an updated version of the land surface model, called Minimal  
346 Advanced Treatments of Surface Interaction and RunOff (MATSIRO; Takata et al.  
347 2003), which predicts the temperature and water in six soil layers down to a 14 m depth,  
348 one canopy layer, and three snow layers. In this version of MATSIRO, a tile treatment  
349 of the land surface has been introduced in order to represent the subgrid fraction of land  
350 surface types. One land surface grid is divided into 3 tiles in the control run: potential  
351 vegetation, cropland, and lake. All the prognostic and diagnostic variables are calculated  
352 in each tile, and the fluxes at the land surface are averaged using their fractional weights.  
353 Other modifications from the previous version are briefly described below.

354

##### 355 1) Lake submodel

356 We calculate the surface heat and water fluxes over lakes as one of the tiles in a  
357 grid. The water temperature and mass are predicted for the surface layer (minimum  
358 thickness of 1 m) and four levels, based on the thermal diffusion and mass conversion,  
359 considering vertical overturning, evaporation, precipitation, and inflow from and  
360 outflow to rivers. The distribution and fraction of lakes are fixed in time.

361

##### 362 2) River routing

363 The river routing model is basically the same as that in MIROC3 except for the  
364 updated river network for the T85 resolution (Yamazaki et al. 2009) and the method for

365 calculating the river discharge (Oki et al. 2003)

366

### 367 3) Snow and ice albedo

368 The aging effect on snow albedo is considered in MATSIRO following Yang et  
369 al. (1997). Among the three coefficients that affect the increment in the non-  
370 dimensional age of snow, the one representing the effect of dirt increases by referring to  
371 its concentration in the surface snow layer. This mimics the observed relation between  
372 snow albedo and dirt concentration (Aoki et al. 2006). The dirt concentration is  
373 calculated from the deposition fluxes of dust and soot in SPRINTARS. Since the  
374 absorption coefficients of dust and soot are very different, the deposition fluxes are  
375 multiplied by their relative weights (0.012 for soil dust and 0.988 for black carbon). The  
376 sum is used as the radiatively effective deposition of dust and soot.

377 The previous version of MATSIRO assumed constant values for the surface  
378 albedo over an ice sheet. This has been changed in the present version following  
379 Bougamount et al. (2005), who proposed that the ice-sheet albedo be expressed as a  
380 function of the water content above the ice. This scheme is applicable for both visible  
381 and near-infrared radiation, with a fixed value of 0.05 being used for the infrared band.

382

### 383 *e. Control experiment*

#### 384 1) Boundary conditions

385 The historical changes in the total solar irradiance and in volcanic aerosol optical  
386 depth in the stratosphere are given by Lean et al. (2005) and Sato et al. (1993),  
387 respectively. The former is set to  $1365.7 \text{ W m}^{-2}$ , and the latter, including its seasonal  
388 change in latitude and height, is fixed at the value for the year 1850 for the control



simulation. The atmospheric concentrations of well-mixed greenhouse gases and the surface emissions of tropospheric aerosols are provided by an international task group, “RCP Concentration Calculations and Data”<sup>1</sup>. The concentrations of CO<sub>2</sub>, CH<sub>4</sub>, and N<sub>2</sub>O are set to 284.725 ppm, 790.979 ppb, and 275.425 ppb, respectively. The three-dimensional atmospheric concentrations of ozone are pre-calculated by a chemistry climate model called CHASER (Sudo et al. 2002), driven with emissions of its precursors in the 1850 condition given by the task group.

The boundary conditions for the land module consist of the fractions of three tiles (potential vegetation, cropland, and lake), the distribution of potential vegetation, and the leaf area index (LAI). The historical land use change is given by the land use harmonization data (Hurtt et al. 2009), in which the cropland fraction is fixed at the value in 1850 for the control simulation. The lake fraction is based on the U.S. geological survey global land cover characterization dataset. The potential vegetation data are prepared on the basis of the SAGE dataset (Ramankutty and Foley, 1999) and interpreted for the MATSIRO vegetation types. Since the SAGE data do not include C4 vegetation and permanent ice distribution, they are estimated from ISLSCP2 C4 vegetation data (Still et al. 2003) and MODIS snow cover data for 2001–2007 (Hall et al. 2006), respectively. The LAI data are prepared from the MODIS LAI products (Shabanov et al. 2005) by separating the LAI into two tiles using the HYDE3 land use data (Goldewijk et al. 2007) to detect the cropland LAI in the MODIS data. The effect of the historical land-use change on LAI is taken into account by changing fractions between the potential vegetation and cropland in the tile treatment.

---

<sup>1</sup> <http://www.pik-potsdam.de/~mmalte/rcps/index.htm>

## 412 2) Tuning and spin-up procedures

413 The atmospheric component is run for 10 y from an initial state obtained from  
414 the MIROC3 control simulation. The ocean and sea ice components are spun up for 530  
415 y from the initial states provided by the Polar Science Center hydrographic climatology  
416 (PHC3.0, Steele et al. 2001). Acceleration is applied to the abyssal dynamical fields  
417 except for the last 20 y, in order to obtain quasi-equilibrium during the spin up. After  
418 the component models are coupled, we further integrate MIROC5 for about a thousand  
419 years, during which parameters in cloud, convection, turbulence, aerosol, and sea ice  
420 schemes are perturbed to find the best set that results in a realistic climate. The number  
421 of parameters (less than 20) and the range of their perturbations were subjectively  
422 determined by experts as in the physics ensemble experiment (Yokohata et al. 2010).

423 The strategy of the model tuning follows that adopted for developing MIROC3,  
424 and is conventional. Specifically, the model's time-mean states are compared at every 5  
425 y in addition to monitoring the global-mean time series of several important quantities  
426 (e.g., SST, surface air temperature (SAT), and the top of the atmosphere (TOA)  
427 radiative fluxes). While we have not employed a quantitative metric to rate the model's  
428 performance (Reichler and Kim 2008), the biases of many atmosphere and ocean  
429 variables are evaluated in terms of their global means and spatial patterns at each tuning  
430 cycle. This type of tuning is sometimes criticized because the same set of observational  
431 data is used for tuning and validation. However, the bias structure is complex, as will be  
432 shown later, and the parameter values are uniform both in time and space. Thus, we  
433 cannot control the model biases in an artificial manner when the global means of the  
434 primary variables (i.e., radiative budgets and temperature) are tuned to be close to the  
435 observations.

436           Figure 1 shows the global mean SST, along with the ocean temperature averaged  
437 for the upper 700 m and for the entire depth level (denoted as VAT700 and VAT,  
438 respectively) during 2001 and 2300 (the year label does not have any particular  
439 meaning). Note that the parameter values have been fixed for the 300-y periods. SST  
440 and VAT700 time series indicate that the upper ocean is close to equilibrium at least  
441 after 2100, but the deep ocean still warms very slowly as confirmed by VAT. While  
442 further several hundred years may be required to obtain a fully equilibrated state, we use  
443 the climatological mean fields obtained from the 100-y average during 2101 and 2200  
444 in this paper.

445           To validate the model climatology and variability, we use observational data sets.  
446 The primary data are derived from Ishii et al. (2006), who provide the SST, sea surface  
447 salinity (SSS), their subsurface fields, and sea ice concentration for 1945–2006. The  
448 climatology of the atmospheric and the precipitation fields are respectively obtained  
449 from the European Centre for Medium Range Weather Forecasts (ECMWF) 40-y  
450 reanalysis (ERA40, Uppala et al. 2005) and the CPC merged analysis of precipitation  
451 (CMAP, Xie and Arkin 1997). Several satellite products are also used for validating the  
452 radiative budgets, precipitation, and cloud fields. These data are described when  
453 referred to in the subsequent sections.

454           Care should be taken to use the instrumental measurements for recent decades to  
455 validate the pre-industrial climate simulated in CTL because of the difference in  
456 radiative forcing. Ideally, the model climate should be compared with observations by  
457 performing the 20<sup>th</sup> century historical experiment (20C run), and then, the model initial  
458 state in 1850 should be calculated backward in time (e.g., Stouffer et al. 2004).  
459 However, because such a method is computationally expensive, we first carried out a

pre-industrial experiment. This is justified by the fact that the differences in the mean state between CTL and the 20C run are smaller than the model biases identified in CTL. Indeed, we found that the differences in the global-mean precipitation and SST between the CTL climatology and the 1961–1990 average obtained from the 20C run using MIROC5 were  $-0.016 \text{ mm dy}^{-1}$  and  $0.13 \text{ K}$ , respectively. Even at the grid scale, the differences range only from  $-1.5$  to  $0.9 \text{ mm dy}^{-1}$  and from  $-1.5$  to  $0.9 \text{ K}$ , which are much smaller than the ranges of the corresponding biases (Figs. 4 and 6).

### 3. Mean states and variability

#### *a. Global mean budgets*

A brief comparison is made for the global mean radiative budgets at the TOA, temperature, and hydrological quantities between the observed estimates and two models (Table 1). The observed radiative budgets contain uncertainties, so two different estimates are listed. The solar insolation depends only on the solar constant, and thus the values from the observations and models are almost identical. On the other hand, the TOA net incoming shortwave (SW) and outgoing longwave (LW) fluxes vary among models, and even between two observational estimates. The SW flux in MIROC3med ( $235.7 \text{ W m}^{-2}$ ) is similar to the estimate from ISCCP ( $235.8 \text{ W m}^{-2}$ , Zhang et al. 2004). Both MIROC3hi ( $240.0 \text{ W m}^{-2}$ ) and MIROC5 ( $237.6 \text{ W m}^{-2}$ ) show a larger net SW flux closer to the recent CERES estimate ( $240.5 \text{ W m}^{-2}$ , Loeb et al. 2009). It should be noted that the net flux in MIROC5 denotes a negative value slightly larger than that in MIROC3. This will mostly come from the spin-up of abyssal ocean and gradually approach equilibrium (the linear trend is  $0.07 \pm 0.04 \text{ W m}^{-2}$  per century for the last 100 y).

484 Global cloud radiative forcing (CRF) reveals a different property from the net  
485 fluxes. The cooling effect due to SW CRF in MIROC3med and MIROC5 (both  $-53.8 \text{ W m}^{-2}$   
486  $\text{m}^{-2}$ ) is stronger than that in MIROC3hi ( $-48.7 \text{ W m}^{-2}$ ) by about  $5 \text{ W m}^{-2}$  whereas the  
487 warming due to LW CRF is slightly weaker in MIROC5 ( $26.3 \text{ W m}^{-2}$  against  $27.0\text{--}27.6$   
488  $\text{W m}^{-2}$  in MIROC3). The net CRFs in MIROC3med ( $-26.2 \text{ W m}^{-2}$ ) and MIROC5 ( $-27.5$   
489  $\text{W m}^{-2}$ ) are similar to each other, which that in MIROC3hi is weaker ( $-21.7 \text{ W m}^{-2}$ ).  
490 Referring to the net CRF difference between the two observational estimates (more than  
491  $7 \text{ W m}^{-2}$ ) shows that the difference between the three models may not be large. As will  
492 be shown in section 4, a similar magnitude for the net CRF does not imply a similar  
493 cloud feedback in a climate change simulation.

494 The global mean SAT and SST are also presented in Table 1. As compared with  
495 observations by Jones et al. (2001), the mean temperature is cold by  $0.6\text{--}0.8 \text{ K}$  in  
496 MIROC3med while close but slightly cooler, by  $0.1\text{--}0.4 \text{ K}$ , in MIROC3hi. In contrast,  
497 the MIROC5 climate is somewhat warm with the SAT  $0.5 \text{ K}$  warmer than the observed  
498 value in Jones et al.'s data, even though the value is nearly identical to ERA40.

499 The atmospheric water budgets (precipitation minus evaporation) are strictly  
500 balanced in all the models. The global mean precipitation is excessive in MIROC5,  
501 suggesting a hydrological cycle that is too active. This may partly be due to a warmer  
502 mean state, which will also result in more cloud production. The total cloud cover is the  
503 largest in MIROC5 (56.3%) which is closer to observation (60%).

504

#### 505 ***b. Climatological fields***

506 The climatological radiative budgets at TOA in MIROC5 are displayed in Fig.  
507 2a,d. Unless otherwise stated, the model climatological states are compared with

508 observations on an annual mean basis. The horizontal average values of the net outgoing  
509 LW (Fig. 2a) and incoming SW (Fig. 2d) are shown in Table 1. Overall, the distribution  
510 is realistic; yet, their differences from the Earth Radiation Budget Experiment (ERBE;  
511 Barkstrom 1984) climatology indicate a systematic radiation bias (Fig. 2c,f). Both SW  
512 and LW are excessive in high latitudes of about  $40^{\circ}$ – $65^{\circ}$ , whereas the solar insolation is  
513 insufficient over the tropical oceans. For comparison, similar bias maps for  
514 MIROC3med are shown in Fig. 2b,e. On one hand, the LW bias is reduced in MIROC5,  
515 especially over the tropics. This is due to an improvement in high clouds in association  
516 with the deep convections. On the other hand, the SW bias in MIROC5 is generally  
517 larger than that in MIROC3med. In particular, the deficient insolation over the tropical  
518 oceans reflects that low clouds are overrepresented. The large bias near the equator in  
519 MIROC3med (Fig. 2e) is less in MIROC5, but a negative bias over the subtropical  
520 western Pacific is worse instead. We tested a parameterization for cloud-top entrainment  
521 instability (CTEI), which works to remove the excessive low clouds. However, it is  
522 arguable if CTEI is so active as to dissipate the boundary layer cloud over a wide area  
523 of the tropics, so we turned it off in the control experiment.

524         Figure 3 shows the mean SST from observations and MIROC5. The warm pool  
525 in the Indo-Pacific region well extends to the west and east of the maritime continent.  
526 As compared with the observations and MIROC3 (not shown), the meridional width of  
527 the warm pool in MIROC5 is somewhat narrower, but the SST around the date line is  
528 still high enough to affect the ENSO simulation. The modeled zonal SST gradient in the  
529 equatorial Atlantic is opposite to the observations, which is a common error of the  
530 current generation CGCMs (Richter and Xie 2008).

531         The SST and SSS biases are compared between MIROC3med and MIROC5

532 (Fig. 4). In MIROC3med, a cooling bias is found in a wide area of the ocean, except for  
533 the eastern periphery of each ocean basin and the Antarctic Ocean, where a warming  
534 bias dominates (Fig. 4a). The bias in SSS is positive (negative) in the western equatorial  
535 Pacific (eastern Indian Ocean and the tropical Atlantic), and especially large in the  
536 Arctic Ocean (Fig. 4b). The SST bias in MIROC5 is reduced in low latitudes, but  
537 amplified in the North Pacific and in the Antarctic Ocean (Fig. 4c). The bias in the  
538 North Pacific is likely due to surface westerly shifted southward in the atmosphere  
539 model. The warming bias in the southern polar region may partly be reduced when the  
540 deep ocean is fully spun up. While the root-mean-square error of SST in MIROC5 is 1.5  
541 K, which is only slightly smaller than the value in MIROC3med (1.6 K), the error  
542 reduction is more evident for the tropics (20° S–20° N), where the error is 1.2 K in  
543 MIROC5 and 1.5 K in MIROC3med. Although the SSS biases in the two models are  
544 relatively similar, the bias is slightly smaller in MIROC5 (Fig. 4d).

545       As compared with the CMAP climatology (Fig. 5a), the precipitation pattern  
546 simulated in MIROC5 appears to have a sharp contrast between the heavy precipitation  
547 regions such as the inter-tropical convergence zone (ITCZ) and the surrounding areas.  
548 The mean precipitation in MIROC5 is realistic overall, but a deficiency is seen by  
549 taking the difference from CMAP (Fig. 6). It is known that MIROC3 fails to produce  
550 rich precipitation along the South Pacific convergence zone and over the western and  
551 eastern sides of the maritime continent (Fig. 6a,b). It also shows a double-ITCZ  
552 structure as revealed by the positive bias to the south of the equator over the eastern  
553 Pacific. These shortcomings are greatly diminished in MIROC5, which, instead, shows  
554 the ITCZ that is too strong, accompanied by weak precipitation over the western  
555 equatorial Pacific (Fig. 6c). A positive bias around 60° S is also amplified. It is

556 noticeable that the bias pattern in MIROC5 is considerably different from that in  
557 MIROC3med, which is similar to the bias in MIROC3hi (Fig. 6b). This clearly indicates  
558 that replacing the atmospheric physics package (convection scheme in particular), as  
559 well as the changes in the other component models, had a drastic impact on the model  
560 bias. In contrast, increasing the horizontal resolution, at least from T42 to T106, does  
561 not alter the large-scale bias pattern in MIROC3.

562 Another feature of the precipitation in MIROC5 is a topographically generated  
563 precipitation over continents (e.g., south of the Himalayas, Fig. 5b). This, however, may  
564 not be well resolved by the CMAP data. In order to validate the small scale features in  
565 the precipitation climatology, a comparison is made of the Jun-July-August (JJA) mean  
566 precipitation over the Asian monsoon region between the Tropical Rainfall  
567 Measurement Mission (TRMM) satellite data<sup>2</sup> and MIROC (Fig. 7). The TRMM PR  
568 data averaged for 1998–2008 provide a detailed picture of the monsoon rainfall  
569 concentrated along narrow mountains (Fig. 7a). MIROC3med that does not resolve such  
570 a narrow topography yields loose precipitation climatology broadly representing the  
571 centers of monsoon rainfall, while additional heavy rainfall is observed over oceans (Fig.  
572 7b). The precipitation pattern in MIROC3hi is more confined to narrow regions along  
573 the Western Ghats, Himalayas, and the western Indochina peninsula (Fig. 7c). The  
574 amount of orographically anchored precipitation is much less than the TRMM  
575 precipitation. The mean distributions are qualitatively similar in MIROC3med and  
576 MIROC3hi, but are different from that in MIROC5 (Fig. 7d). Despite the coarser  
577 resolution of MIROC5 when compared to MIROC3hi, it is better at representing the  
578 orographic rainfall over the monsoon region, even overestimated in association with the

---

<sup>2</sup> [http://www.eorc.jaxa.jp/TRMM/index\\_e.htm](http://www.eorc.jaxa.jp/TRMM/index_e.htm)



579 strong hydrological cycle (cf. Table 1). The shortcomings of the precipitation pattern in  
580 MIROC5 are too heavy rainfall over southern China and insufficient rainfall to the west  
581 of the Philippines, which is also seen in MIROC3hi.

582         The zonal mean climatological fields of the zonal wind, temperature, and  
583 specific humidity, along with their biases, are presented in Fig. 8. In MIROC3med, the  
584 SH jet is shifted southward, and a cold (dry) bias near the tropopause (above the  
585 boundary layer) is conspicuous (Fig. 8a,c,e). These are all improved considerably in  
586 MIROC5 (Fig. 8b,d,f). One may wonder if this improvement is due to the doubled  
587 resolution of the atmosphere model. However, the biases in MIROC3med are similarly  
588 found in MIROC3hi, indicating that they come from the formulae in the  
589 parameterization schemes. We found that the updated radiation, turbulence, and cloud  
590 schemes all act to reduce the temperature and moisture biases.

591         In addition to the SST (Fig. 3), the zonal wind stress ( $\tau_x$ ) and ocean subsurface  
592 states, which play a vital role in the ENSO simulation, should be validated. The annual  
593 means of  $\tau_x$  and SST along the equator are plotted in Fig. 9a,b. It is apparent that the  
594 Pacific trades are underestimated in MIROC3med, but are very close to the observations  
595 in MIROC5. The mean SST in the central equatorial Pacific is underestimated in both  
596 models, yet the SST gradient is slightly larger in MIROC5. As also found in Fig. 3, the  
597 zonal SST gradient in the models is reversed in the Atlantic.

598         The observed subsurface temperature climatology is obtained from Ishii et al.  
599 (2006). Because there is no gridded subsurface current data set, we use the assimilation  
600 products of SODA data for the 1958–1999 climatology (Carton and Giese 2008). The  
601 observations in the Pacific are characterized by a contrast between the warm pool  
602 extending down to 100 m in the west, and an eastern Pacific cold region where

603 upwelling cools the subsurface, as well as by a strong EUC having an eastward velocity  
604 greater than  $80 \text{ cm s}^{-1}$  (Fig. 9c). The subsurface temperature climatology in both models  
605 appears similar to each other. However, a careful comparison shows that the  
606 temperature in the central Pacific at around 100 m is warmer in MIROC5, resulting in  
607 the larger zonal gradient to the east (Fig. 9d,e). This difference is consistent with the  
608 EUC being shifted westward and weaker ( $\sim 30 \text{ cm s}^{-1}$ ) in MIROC3med while in  
609 MIROC5 it is located at around  $140^\circ\text{W}$ , as in the SODA climatology, and intensified  
610 ( $\sim 40 \text{ cm s}^{-1}$ ). Since the horizontal resolutions of the ocean models are identical, this  
611 change is attributed mainly to the different advection schemes used in the ocean model  
612 and indirectly to the atmosphere model. The EUC in MIROC5 is still too weak, which  
613 should be closer to the SODA data if we use a higher resolution ocean component.

614         The Arctic and Antarctic sea ice concentrations are shown in Fig. 10. In the NH,  
615 the sea ice fraction in MIROC resembles the observations in both the winter (January–  
616 March) and summer (July–September) seasons, except for an underestimation over the  
617 Okhotsk Sea and off Newfoundland in winter and off the shores of Eurasia and Alaska  
618 in summer. A large bias is found in the SH, where the sea ice is always less than  
619 observed around Antarctica. This bias is worse than MIROC3 and appears to be related  
620 to the amplified warm bias in SST (Fig. 4). Since the deep ocean is still weakly drifting,  
621 a slow warming of the abyssal layer may eventually stimulate convection, which works  
622 to reduce the SH bias. While the figure is not presented, we also compared the seasonal  
623 cycle of the sea ice concentration. Again, the NH sea ice extent is remarkably well  
624 simulated but both the annual mean and amplitude of the seasonal cycle are  
625 underestimated in SH.

626         The Arctic sea ice thickness field in MIROC5 has a maximum along the

627 Canadian coast and the northern coast of Greenland (not shown). This spatial pattern,  
628 also found in MIROC3hi, is improved from MIROC3med, in which the sea ice along  
629 the Siberian coast was thicker.

630

### 631 *c. Variability*

632 Among the various aspects of the natural variability, we choose several  
633 phenomena as examples to discuss the simulated perturbations arising from the  
634 atmosphere and ocean, and their coupling: namely, the Atlantic meridional overturning  
635 cell (AMOC), equatorial waves, and ENSO. A full description of these modes of  
636 variability in MIROC5 and their sensitivity to parameters will be reported elsewhere  
637 (Watanabe et al. 2010; Chikira and Sugiyama 2010, in preparation).

638 Figure 11 compares the mean AMOCs and their fluctuations. The AMOC  
639 intensity is measured by the maximum transport in the North Atlantic and the transport  
640 at the equator (Fig. 11c,d). It turns out that MIROC5 generates a somewhat strong  
641 AMOC, which has a maximum transport of about 22 Sv and a transport of about 17 Sv  
642 at the equator. These are stronger by about 2 Sv than those in MIROC3med. Because of  
643 observational uncertainty, it is not clear which is more realistic. The AMOC in  
644 MIROC5 shows a slight weakening tendency during this period, but it again gradually  
645 strengthens in the next 100 y (not shown). In association with the AMOC variability, we  
646 also analyzed the time series and spatial pattern of the Atlantic multidecadal oscillation  
647 (AMO). When compared with observations (Trenberth and Shea 2006), both  
648 MIROC3med and MIROC5 well reproduced a horseshoe pattern in the annual-mean  
649 SST anomalies in the North Atlantic (not shown). The variances of the AMO time series  
650 were similar between MIROC3med and MIROC5 (0.14 and 0.16 K), but the time scale

651 of the variability was somewhat shorter in MIROC3med than in MIROC5, with the  
652 latter comparable to the observations.

653         The property of equatorial waves in the atmosphere is examined by calculating  
654 zonal wavenumber-frequency power spectra for the symmetric component of the  
655 outgoing longwave radiation (OLR), following the procedure proposed by Wheeler and  
656 Kiladis (1999). The daily mean OLR data derived from the Advanced Very High  
657 Resolution Radiometer (AVHRR) of the NOAA satellites for 1979–2005 (Liebmann  
658 and Smith 1996) are used for observational references, which show well-separated  
659 signals corresponding to the Madden-Julian oscillation as well as the equatorial Rossby  
660 and Kelvin waves (Fig. 12a). The overall spectra are similar between MIROC3 and  
661 MIROC5 (Fig. 12b–d), but the equatorial Kelvin waves are overrepresented  
662 (underrepresented) in MIROC3 (MIROC5). In particular, both MIROC3med and  
663 MIROC3hi simulate too much of the high-frequency Kelvin waves having a deep  
664 equivalent depth. It is noticeable that the power spectrum in MIROC5 exhibits a distinct  
665 peak akin to the observed MJO even though it includes perturbations with smaller zonal  
666 scales (Fig. 12d). Further exploration of the modeled intraseasonal variability is beyond  
667 the scope of this paper, but Fig. 12 strongly suggests that the MJO is better reproduced  
668 in MIROC5.

669         As mentioned in the introduction, MIROC3 was not able to simulate sufficient  
670 ENSO amplitude, although the zonal gradient of the mean thermocline was realistic  
671 (Guilyardi et al. 2009a). Fortunately, this deficiency is greatly improved in MIROC5. In  
672 Fig. 13 we compare the ENSO amplitudes as measured by the Niño 3 SST anomalies  
673 between the observations and two models. As evident from the time series and the  
674 standard deviation (SD), the ENSO amplitude in MIROC3med is roughly half that

675 observed; it is even weaker in MIROC3hi (Fig. 13b,c). In MIROC5, ENSO is much  
 676 more realistic in terms of the amplitude and asymmetry between El Niño and La Niña  
 677 (Fig. 13d). The SD is nearly identical to the observations, but this is partly coincidental  
 678 because the SD varies from 0.64 to 0.99 K when sampling different 100-y periods  
 679 between 2001 and 2300. The ENSO periodicity was also examined using the power  
 680 spectrum of the Niño 3 SST anomalies (not shown). A comparison of the spectra shows  
 681 that the ENSO in MIROC5 has clear double peaks at 4.3 and 5.3–6.7 y, which are  
 682 respectively close to the observed peaks at 3.7 and 5.2 y for the 1945–2006 period. In  
 683 contrast, the ENSO in MIROC3med has a broad single peak at around 4–10 y.

684         Figure 14 illustrates the monthly anomalies regressed on the Niño 3 time series  
 685 shown in Fig. 13a,d. The global SST anomaly pattern associated with the ENSO in  
 686 MIROC5 is remarkably similar to the observations (Fig. 14a,d). The negative  
 687 precipitation anomaly over the western tropical Pacific is somewhat underestimated, but  
 688 the extratropical response to ENSO is also very realistic (Fig. 14c,f).

689         A full explanation of why MIROC5 simulates ENSO much better than MIROC3  
 690 is difficult because of the complexity of the ENSO dynamics. One possible reason is the  
 691 intensified atmosphere-ocean coupling, as measured by the so-called coupling feedback  
 692 parameter,  $\mu$ , which is defined by the regression slope of  $\tau_x$  anomalies over the Niño 4  
 693 region upon the Niño 3 SST anomalies (Guilyardi et al. 2009b). A scatter plot of these  
 694 two quantities exhibits that in MIROC5,  $\mu$  is twice as large as in MIROC3med (Fig. 15),  
 695 and lies within the observational estimate of  $\mu = 8.6\text{--}12.8 \times 10^{-3} \text{ N m}^{-2} \text{ K}^{-1}$  (cf. Guilyardi  
 696 et al. 2009b). The realistic intensity of the wind stress response to the SST anomaly will  
 697 be related to the improved zonal profile of mean  $\tau_x$  (Fig. 9a). We performed several  
 698 additional experiments in which the ENSO amplitudes were found to be sensitive to the

699 change in a parameter that affects the efficiency of the cumulus entrainment. This  
700 convective control of ENSO has been fully investigated and reported in a separate paper  
701 (Watanabe et al. 2010).

702

#### 703 **4. Climate sensitivity**

704 One of the lessons from the CMIP3 is the necessity of using a variety of metrics  
705 to evaluate the errors in CGCMs. This implies that a model representing reasonable  
706 climate mean states ensures neither realistic internal variability nor reliable climate  
707 sensitivity (e.g., Knutti and Hegerl 2008). Therefore, in this section we perform a  
708 preliminary examination of the equilibrium climate sensitivity in MIROC5.

709 As a prelude to the climate sensitivity analysis, we compare cloud properties that  
710 are crucial in determining the sensitivity to radiative forcing between MIROC and  
711 satellite estimates that have recently become available. First, the upper tropospheric  
712 cloud ice contents obtained from the control runs in MIROC3med and MIROC5 are  
713 presented together with the annual mean of two satellite estimates (Fig. 16; partly  
714 reproduced from Waliser et al. 2009). Since the Aura/Microwave Limb Sounder (MLS)  
715 and CloudSat products are available only for 2007 and from August 2006 to July 2007,  
716 respectively, full comparisons with satellite climatology are not possible. Yet, a  
717 tendency for MIROC3 to produce excessive cloud ice is clearly seen, whereas MIROC5  
718 generates a more reasonable amount of ice content (Fig. 16c,d). The lack of cold rain  
719 processes in MIROC3 might explain why the old model overestimates cloud ice.

720 Representation of the cloud liquid/ice partitioning is a more severe test of a  
721 model's cloud scheme. The fraction of cloud liquid to total cloud condensate  
722 (liquid+ice), denoted as  $F_{\text{liq}}$ , may follow the temperature in the environment, as has

723 been assumed in MIROC3, but will also depend on microphysical processes. The  
 724 observed  $F_{\text{liq}}$  is estimated from the Cloud-Aerosol Lidar Infrared Pathfinder Satellite  
 725 Observations (CALIPSO) derived from algorithms by Yoshida et al. (2010), and is  
 726 compared with the MIROC5 outputs. Because of the too short period of satellite data,  
 727 more significance is obtained via latitudinal distributions of  $F_{\text{liq}}$  as a function of  
 728 temperature but not geographical maps (Fig. 17). As anticipated, the  $F_{\text{liq}}$  in CALIPSO  
 729 gradually decreases for lower temperatures, but is high over the subtropics and polar  
 730 latitudes (Fig. 17a). The average temperature when the amount of cloud liquid and ice is  
 731 equal ( $F_{\text{liq}} = 0.5$ ) is about  $-10^{\circ}\text{C}$ . While the reason is not yet clear, MIROC5 does well  
 732 reproducing the latitudinal distribution of  $F_{\text{liq}}$  (Fig. 17b). A wavy pattern near the  
 733 equator is due to insufficient number of samples for  $T < 0^{\circ}\text{C}$  and is not concerned. It  
 734 should be noted that a given function of  $F_{\text{liq}}$  in MIROC3 was set so that  $F_{\text{liq}} = 0.5$  at  $T =$   
 735  $-7.5^{\circ}\text{C}$ , and was tuned from a standard function of  $F_{\text{liq}} = 0.5$  at  $T = -15^{\circ}\text{C}$ , which  
 736 results in a very high climate sensitivity. The realistic  $F_{\text{liq}}$  as a function of  $T$  in MIROC5  
 737 appears to lead to a better response of the mixed phase cloud to radiative forcing.

738         The equilibrium climate sensitivity, denoted as  $\Delta T_{2\times}$ , is evaluated by using  
 739 initial 20-y products of the CO<sub>2</sub>x4 experiment. From the initial states taken from the  
 740 control integration, the model was re-run with an abruptly increased CO<sub>2</sub> concentration  
 741 of 1138.8 ppm, which is four times the value used in the control run. Because the  
 742 ensemble CO<sub>2</sub>x4 experiment using MIROC5 is still ongoing, the full analysis will be  
 743 done in future work. In order to estimate  $\Delta T_{2\times}$  without an equilibrium calculation,  
 744 which requires a very long integration, we adopt a method proposed by Gregory et al.  
 745 (2004). Given the fact that the relationship between the annual- and global-mean  
 746 radiative flux change (CO<sub>2</sub>x4 minus control) at TOA and the SAT change is well fitted

747 by a straight line,  $\Delta T_{2x}$  can be obtained at the intersection of the regression curve with  
748 the horizontal axis (i.e., extrapolation to the equilibrium state), divided by 2. Gregory et  
749 al.'s method is very convenient for estimating  $\Delta T_{2x}$  using a transient time evolution in  
750 the CO<sub>2</sub>x4 experiment with full CGCMs.

751 The regression of the TOA net radiation change on the SAT change is presented  
752 in Fig. 18 (black line), where  $\Delta T_{2x}$  is estimated at 3.6 and 2.6 K in MIROC3med and  
753 MIROC5, respectively. The reduction of the climate sensitivity in MIROC5 arises from  
754 a weakly negative SW feedback due to clouds; it has an opposite sign to that in  
755 MIROC3 (red lines). This is consistent with the previous works showing that the cloud-  
756 SW feedback varies the most among CGCMs (e.g., Bony and Dufresne 2005).

757 The cloud-SW feedback in MIROC3 is determined mostly by low clouds  
758 (Yokohata et al. 2010). Therefore, the signs of the cloud-SW feedback suggest that low  
759 clouds decrease by quadrupling the CO<sub>2</sub> in MIROC3, whereas they slightly increase in  
760 MIROC5. The changes in low cloud cover indeed reveal such differences (Fig. 19). The  
761 polar cloud is found to increase in both models and the overall patterns are not  
762 drastically different. However, the low clouds decrease in low latitudes, except for the  
763 off-equatorial Pacific in MIROC3med (Fig. 19a), whereas they increase over the  
764 tropical oceans in MIROC5 (Fig. 19b). The tropical (30° S-30° N) mean change is  
765 +0.84% in MIROC5, compared to -0.62% in MIROC3med. It is interesting that the  
766 subtropical subsidence has weakened in the CO<sub>2</sub>x4 run due to increased static stability;  
767 nevertheless, the boundary layer is thinner in the MIROC5 CO<sub>2</sub>x4 experiment. This  
768 appears to be consistent with the prediction of a simple model by Caldwell and  
769 Bretherton (2009), but further investigation of the mechanism responsible for this low  
770 cloud increase and the resultant negative cloud-SW feedback is beyond the scope of this



771 paper.

772

## 773 **5. Concluding discussion**

774 A new version of the global climate model MIROC was developed for better  
775 simulation of the mean climate, variability, and climate change due to anthropogenic  
776 radiative forcing. A century-long control experiment was performed using the new  
777 version (MIROC5) with the standard resolution of the T85 atmosphere and 1° ocean  
778 models. The climatological mean state and variability were then compared with  
779 observations and those from a previous version (MIROC3) with two different  
780 resolutions, coarser and finer than the resolution of MIROC5.

781 Climatological precipitation and SST improved in MIROC5 in several respects:  
782 a single ITCZ, more realistic zonal SST gradient on the equator, and topographically  
783 anchored precipitation associated with the Asian monsoon (Figs. 3,5,7). A new cumulus  
784 convection scheme and a more accurate advection scheme for ocean currents may be the  
785 major contributors to these improvements. Updated schemes for radiation and  
786 turbulence also work to reduce the zonal-mean biases in temperature and moisture (Fig.  
787 8). It is noticeable that MIROC5 simulates ENSO more realistically than the previous  
788 models, which produced a weak ENSO even with a higher resolution (Figs. 13,14). The  
789 new MIROC employs a prognostic treatment for the cloud water and ice mixing ratio,  
790 as well as the cloud fraction, considering both warm and cold rain processes. Validation  
791 of the model cloud fields using recent satellite data shows that they are better simulated  
792 in MIROC5 than in MIROC3 (Figs. 15,16). MIROC5 reveals an equilibrium climate  
793 sensitivity of 2.6 K, which is 1 K lower than that in MIROC3 (Fig. 17). This is probably  
794 because, in the two versions, the response of low clouds to an increasing concentration

795 of CO<sub>2</sub> is opposite; that is, low clouds decrease (increase) at low latitudes in MIROC3  
796 (MIROC5).

797       The comparison of the two versions of MIROC presented here indicates that the  
798 overall impact on the model climatology of updating the parameterization schemes is  
799 greater than the effect of increasing the model resolution (at least for T106 vs. T85).  
800 This may not be surprising because the high-resolution model used here does not  
801 explicitly resolve some key phenomena such as the convective systems. However, a part  
802 of the model bias will certainly be improved by MIROC3hi. For example, a substantial  
803 cooling bias in the SST is found over the North Atlantic in both MIROC3med and  
804 MIROC5 (Fig. 4a,c). This bias corresponds to a slight displacement of the sharp zonal  
805 SST gradient associated with the Gulf Stream and is reduced in MIROC3hi that adopts  
806 the high-resolution ocean model (not shown). The new physics package in MIROC5 is  
807 also not capable of removing several biases in mean states. In particular, the lack of  
808 heavy precipitation in the west of the Philippines in boreal summer (cf. Fig. 7) may be  
809 crucial for the simulation of the tropical cyclone tracks associated with the subtropical  
810 high in the western Pacific.

811       The simulation of the climate variability and climate change in MIROC5 are  
812 only briefly described in the present paper. The mechanisms and their sensitivity to the  
813 details of the parameterizations will be elaborated upon in subsequent papers. We have  
814 performed several sensitivity experiments, which strongly suggest that the model ENSO  
815 is primarily controlled by the cumulus convection (Watanabe et al. 2010). It is also  
816 suggested from a series of aqua-planet experiments that the equilibrium climate  
817 sensitivity, which is qualitatively different from that in the previous model version, can  
818 be attributed to the different treatment of clouds and cloud microphysics.

819           A possible extension of MIROC5 in the next stage may be the incorporation of  
820 modules, e.g., carbon and chemistry cycles, dynamic vegetation, etc, required for the  
821 ESM. Before such an extension, however, we plan to extensively use MIROC5 for  
822 mechanism studies to understand natural climate variability, and for a series of the near-  
823 term climate prediction experiments designed in the Coupled Model Intercomparison  
824 Project 5 (CMIP5) (details of the CMIP5 experiments are available at [http://cmip-](http://cmip-pcmdi.llnl.gov/cmip5/experiment_design.html)  
825 [pcmdi.llnl.gov/cmip5/experiment\\_design.html](http://cmip-pcmdi.llnl.gov/cmip5/experiment_design.html)). The better simulation of the ENSO and  
826 other modes of variability, as well as improved mean states, will increase the fidelity of  
827 the near-term prediction, which is affected not only by anthropogenic radiative forcing  
828 but also by intrinsic fluctuations in the climate system.

829

830 ***Acknowledgments.*** We are grateful to the three anonymous reviewers for their useful  
831 comments. H. Okamoto of the Kyushu University is appreciated for providing  
832 unpublished results of the CALIPSO products. Thanks are also due to our colleagues in  
833 the MIROC modeling group: T. Nagashima, M. Abe, and H. Kawase for compiling the  
834 external input data: A. Oka and H. Shiogama for drawing some figures: and M.  
835 Yoshimori for running the CO<sub>2</sub>x4 experiment. T. Tozuka, Y. Takayabu, and N. Hirota  
836 helped in collecting some of the observed data. This work was supported by the  
837 Innovative Program of Climate Change Projection for the 21<sup>st</sup> Century (“Kakushin”  
838 program) from MEXT, Japan. The computation was carried out on the Earth Simulator.

839

840 REFERENCES

841

842 Aoki, T., H. Motoyoshi, Y. Kodama, T. J. Yasunari, K. Sugiura, and H. Kobayashi,  
843 2006: Atmospheric aerosol deposition on snow surfaces and its effect on albedo.  
844 *SOLA*, **2**, 13-16, doi:10.2151/sola.2006-004.

845 Arakawa, A., and W. H. Schubert, 1974: Interaction of a cumulus cloud ensemble with  
846 the large-scale environment. *J. Atmos. Sci.*, **31**, 674-701.

847 Arakawa, A., and C. S. Konor, 1996: Vertical differencing of the primitive equations  
848 based on the Charney-Phillips grid in hybrid  $\sigma$ -p vertical coordinates. *Mon. Wea.*  
849 *Rev.*, **124**, 511-528.

850 Barkstrom, B. R., 1984: The Earth Radiation Budget Experiment (ERBE). *Bull. Amer.*  
851 *Meteor. Soc.*, **65**, 1170-1185.

852 Bestsen, M., G. Evensen, H. Drange, and D. Jenkins 1999: Coordinate transformation  
853 on a sphere using conformal mapping. *Mon. Wea. Rev.*, **127**, 2733-740.

854 Bitz, C. M., and W. H. Lipscomb, 1999: An energy-conserving thermodynamic model  
855 of sea ice. *J. Geophys. Res.*, **104**, 15669-15677.

856 Bitz, C. M., M. M. Holland, A. J. Weaver, and M. Eby, 2001: Simulating the ice-  
857 thickness distribution in a coupled climate model. *J. Geophys. Res.*, **106**, 2441-  
858 2463.

859 Bony, S., and J. L. Dufresne, 2005: Marine boundary layer clouds at the heart of  
860 tropical cloud feedback uncertainties in climate models. *Geophys. Res. Lett.*, **32**,  
861 L20806, doi:10.1029/2005GL023851.

862 Bougamont, M., J. L. Bamber, and W. Greuell, 2005: A surface mass balance model for  
863 the Greenland ice sheet. *J. Geophys. Res.*, **110**, F04018,  
864 doi:10.1029/2005JF000348.

865 Caldwell, P., and C. S. Bretherton, 2009: Response of a subtropical stratocumulus-  
866 capped mixed layer to climate and aerosol changes. *J. Climate*, **22**, 20-38.

867 Carton, J. A., and B. S. Giese, 2008: A reanalysis of ocean climate using simple ocean  
868 data assimilation. *Mon. Wea. Rev.*, **136**, 2999-3017.

869 Chikira, M., and M. Sugiyama, 2009: A cumulus parameterization with state-dependent  
870 entrainment rate. Part I: Description and sensitivity to temperature and humidity  
871 profiles. *J. Atmos. Sci.*, in press.

872 Chikira, M., 2009: A cumulus parameterization with state-dependent entrainment rate.  
873 Part II: Impact on climatology in a general circulation model. *J. Atmos. Sci.*,  
874 submitted.

875 Emori, S., A. Hasegawa, T. Suzuki, and K. Dairaku, 2005: Validation,  
876 parameterization dependence and future projection of daily precipitation simulated  
877 with a high-resolution atmospheric GCM. *Geophys. Res. Lett.*, **3**, L06708,  
878 doi:10.1029/2004GL022306.

879 Gent, P. R., J. Willebrand, T. J. McDougall, and J. C. McWilliams, 1995:  
880 Parameterizing eddy-induced tracer transports in ocean circulation models. *J. Phys.*  
881 *Oceanogr.*, **25**, 463-474.

882 Gent, P. R., S. G. Yeager, R. B. Neale, S. Levis, and D. A. Bailey, 2009: Improvements  
883 in a half degree atmosphere/land version of the CCSM. *Clim. Dyn.*,  
884 doi:10.1007/s00382-009-0614-8.

885 Goldewijk, K. K., A. F. Bouwman, and G. van Drecht 2007. Mapping contemporary  
886 global cropland and grassland distributions on a 5 by 5 minute resolution. *Journal*  
887 *of Land Use Science*, **2**, 167-190

888 Gregory, D., 2001: Estimation of entrainment rate in simple models of convective  
889 clouds. *Quart. J. Roy. Met. Soc.*, **127**, 53-72.

890 Gregory, J. M., and Coauthors, 2004: A new method for diagnosing radiative forcing  
891 and climate sensitivity. *Geophys. Res. Lett.*, **31**, doi:10.1029/2003GL018747.

892 Guilyardi E., A. Wittenberg, A. Fedorov, M. Collins, C. Wang, A. Capotondi, G. J. van  
893 Oldenborgh, and T. Stockdale, 2009a: Understanding El Niño in ocean-atmosphere  
894 general circulation models: Progress and challenges. *Bull. Amer. Met. Soc.*, **90**,  
895 325-340.

896 Guilyardi, E., P. Branconnot, F.-F. Jin, S. T. Kim, M. Kolasinski, T. Li, and I. Musat,  
897 2009b: Atmospheric feedbacks during ENSO in a coupled GCM with a modified  
898 atmospheric convection scheme. *J. Climate*, **22**, 5698-5718.

899 Hall, D. K., G. A. Riggs, and V. V. Salomonson, 2006: MODIS/Terra Snow Cover 8-  
900 Day L3 Global 0.05deg CMG V005, Boulder, Colorado USA: National Snow and  
901 Ice Data Center. Digital media.

902 Hasumi, H., 2006: CCSR Ocean Component Model (COCO) Version 4.0. *CCSR Report*,  
903 **25**, 103pp [available at the Center for Climate System Research, University of  
904 Tokyo].

905 Hurtt, G. C., and Coauthors, 2009: Harmonization of global land-use scenarios for the  
906 period 1500-2100 for IPCC-AR5. *Integrated Land Ecosystem-Atmosphere*  
907 *Processes Study (iLEAPS) Newsletter*, **7**, 6-8.

908 IPCC, 2007: *Climate Change 2007: The Physical Science Basis.*, Cambridge University  
909 Press, 996pp.

910 Ishii, M., M. Kimoto, K. Sakamoto, and S. Iwasaki, 2006: Steric sea level changes  
911 estimated from historical ocean subsurface temperature and salinity analyses. *J.*  
912 *Oceanogr.*, **62**, 155-170.

913 Jones, P. D., and Coauthors, 2001. Adjusting for sampling density in grid box land and  
914 ocean surface temperature time series. *J. Geophys. Res.*, **106**, 3371-3380.

915 Jung, T., S. K. Gulev, I. Rudeva, and V. Soloviv, 2006: Sensitivity of extratropical  
 916 cyclone characteristics to horizontal resolution in the ECMWF model. *Quart. J.*  
 917 *Roy. Met. Soc.*, **13**, 1839-1857.

918 Kiehl, J. T., and K. E. Trenberth, 1997: Earth's annual global mean energy budget. *Bull.*  
 919 *Amer. Meteor. Soc.*, **78**, 197-208.

920 K-1 Model Developers, 2004: K-1 coupled model (MIROC) description. In: Hasumi H,  
 921 Emori S (eds) K-1 technical report. 34 pp [available at the Center for Climate  
 922 System Research, University of Tokyo, <http://www.ccsr.u-tokyo.ac.jp/~agcmadm/>].

923 Knutti, R., and G. Hegerl, 2008: The equilibrium sensitivity of the Earth's temperature  
 924 to radiation changes. *Nature Geosci.*, **1**, 735-743.

925 Large, W. G, G. Danabasoglu, J. C. McWilliams, P. R. Gent, and F. O. Bryan, 2001:  
 926 Equatorial circulation of a global ocean climate model with anisotropic horizontal  
 927 viscosity. *J. Phys. Oceanogr.*, **31**, 518-536.

928 Lean, J., G. Rottman, J. Harder, and G. Kopp, 2005: SORCE contributions to new  
 929 understanding of global change and solar variability. *Solar Phys.*, **230** 27-53.

930 Le Treut, H., and Z. X. Li, 1991: Sensitivity of an atmospheric general circulation  
 931 model to prescribed SST changes: Feedback effects associated with the simulation  
 932 of cloud optical properties. *Clim. Dyn.*, **5**, 175-187.

933 Liebmann, B., and C. A. Smith, 1996: Description of a complete (interpolated) outgoing  
 934 longwave radiation dataset. *Bull. Amer. Meteor. Soc.*, **77**, 1275-1277.

935 Lin, S. J., 2004: A "vertically Lagrangian" finite-volume dynamical core for global  
 936 models. *Mon. Wea. Rev.*, **13**, 2293-2307.

937 Lipscomb, W. H., 2001: Remapping the thickness distribution in sea ice models. *J.*  
 938 *Geophys. Res.*, **106**, 13989-14000.

939 Loeb, N. G., and Coauthors, 2009: Toward optimal closure of the Earth's top-of-

940 atmosphere radiation budget. *J. Climate*, **22**, 748-766.

941 Meehl, G. A., and Coauthors, 2007: The WCRP CMIP3 multimodel dataset. *Bull. Amer.*  
942 *Meteor. Soc.*, **88**, 1383-1394.

943 Mellor, G. L., and T. Yamada, 1974: A hierarchy of turbulence closure models for  
944 planetary boundary layers. *J. Atmos. Sci.*, **31**, 1791-1806.

945 Mellor, G. L., and T. Yamada, 1982: Development of a turbulence closure model for  
946 geophysical fluid problems. *Rev. Geophys. Space Phys.*, **20**, 851-875.

947 Nakamura, T., T. Awaji, T. Hatayama, K. Akitomo, and T. Takizawa, 2000: Tidal  
948 exchange through the Kuril Straits. *J. Phys. Oceanogr.*, **30**, 1622-1644.

949 Nakanishi, M., and H. Niino, 2001: Improvement of the Mellor-Yamada turbulence  
950 closure model based on large-eddy simulation data. *Bound. Layer Meteor.*, **99**,  
951 349-378.

952 Nakanishi, M., and H. Niino, 2004: An improved Mellor-Yamada Level-3 model with  
953 condensation physics: Its design and verification. *Bound. Layer Meteor.*, **112**, 1-31.

954 Nakano, H., and Sugimoto, 2002: Effects of bottom boundary layer parameterization  
955 on reproducing deep and bottom water in a world ocean model. *J. Phys. Oceanogr.*,  
956 **3**, 1209-1227.

957 Noh, Y., and H.-J. Kim, 1999: Simulations of temperature and turbulence structure of  
958 the oceanic boundary layer with the improved near-surface process. *J. Geophys.*  
959 *Res.*, **104**, 15621-15634.

960 Noh, Y., Y. J. Kang, T. Matsuura, and S. Iizuka, 2005: Effect of the Prandtl number in  
961 the parameterization of vertical mixing in an OGCM of the tropical Pacific.  
962 *Geophys. Res. Lett.*, **3**, L23609, doi:10.1029/2005GL024540.

963 Numaguti, A., M. Takahashi, T. Nakajima, and A. Sumi, 1997: Description of  
964 CCSR/NIES atmospheric general circulation model. *CGER's Supercomputer*



965        *Monograph Report, Center for Global Environmental Research, National Institute*  
966        *for Environmental Studies*, **3**, 1-48.

967    Ogura, T., S. Emori, M. J. Webb, Y. Tsushima, T. Yokohata, A. Abe-Ouchi, and M.  
968        Kimoto, 2008: Towards understanding cloud response in atmospheric GCMs: The  
969        use of tendency diagnostics. *J. Meteor. Soc. Japan*, **86**, 69-79.

970    Oki, T., Y. Agata, S. Kanae, T., Saruhashi, and K. Musiake, 2003: Global water  
971        resources assessment under climatic change in 2050 using TRIP. *Water Resources*  
972        *Systems -Water Availability and Global Change, IAHS Publication*, **280**, 124-133.

973    Oouchi, K., J. Yoshimura, H. Yoshimura, R. Mizuta, S. Kusunoki, and A. Noda, 2006:  
974        Tropical cyclone climatology in a global-warming climate as simulated in a 20 km-  
975        mesh global atmospheric model: Frequency and wind intensity analyses. *J. Meteor.*  
976        *Soc. Japan*, **84**, 259-276.

977    Pan, D. M., and D. A. Randall, 1998: A cumulus parameterization with a prognostic  
978        closure. *Quart. J. Roy. Met. Soc.*, **124**, 949-981.

979    Pope, V. D., and R. A. Stratton, 2002: The processes governing horizontal resolution  
980        sensitivity in a climate model. *Clim. Dyn.*, **19**, 211-236.

981    Prather, M. J., 1986: Numerical advection by conservation of second-order moments. *J.*  
982        *Geophys. Res.*, **91**, 6671-6681.

983    Ramankutty, N., and J. A. Foley, 1999: Estimating historical changes in global land  
984        cover: Croplands from 1700 to 1992. *Global Biogeochemical Cycles*, **13**, 997-1027.

985    Reichler, T., and J. Kim, 2008: How well do coupled models simulate Today's climate?  
986        *Bull. Amer. Met. Soc.*, **89**, 303-311.

987    Richter, I., and S.-P. Xie, 2008: On the origin of equatorial Atlantic biases in coupled  
988        general circulation models. *Clim. Dyn.*, **31**, 587-598.

989    Roeske, F., 2001: An atlas of surface fluxes based on the ECMWF reanalysis—A

990 climatological dataset to force global ocean general circulation models. *Max*  
 991 *Planck-Institut fur Meteorologie Rep.*, **33**, 31pp.

992 Sakamoto, T. T., A. Sumi, S. Emori, T. Nishimura, H. Hasumi, T. Suzuki, and M.  
 993 Kimoto, 2004: Far-reaching effects of the Hawaiian Islands in the  
 994 CCSR/NIES/FRCGC high-resolution climate model. *Geophys. Res. Lett.*, **31**,  
 995 L17212, doi:10.1029/2004GL020907.

996 Santer, B. D., and Coauthors, 2009: Incorporating model quality information in climate  
 997 change detection and attribution studie. *PNAS*, **106**, 14778-14783.

998 Sato, M., J. E. Hansen, M. P. McCormick, and J. B. Pollack, 1993: Stratospheric aerosol  
 999 optical depth, 1850-1990. *J. Geophys. Res.*, **98**, 22987-22994.

1000 Semtner, A. J., and R. M. Chervin, 1992: Ocean general circulation from a global eddy-  
 1001 resolving model. *J. Geophys. Res.*, **97**, 5493-5550.

1002 Sekiguchi, M., and T. Nakajima, 2008: A k-distribution-based radiation code and its  
 1003 computational optimization for an atmospheric general circulation model. *J. Quant.*  
 1004 *Spectrosc. Radiat. Transfer*, **109**, 2779-2793.

1005 Shabanov, N. V., and Coauthors, 2005: Analysis and optimization of the MODIS LAI  
 1006 and FPAR algorithm performance over broadleaf forests. *IEEE Trans. in Geo.*  
 1007 *Remote Sensing*, **43**, 1855-1865.

1008 Shaffrey, L. C., and Coauthors, 2009: U.K. HiGEM: The new U.K. high-resolution  
 1009 global environmental model – model description and basic evaluation. *J. Climate*,  
 1010 **22**, 1861-1896.

1011 Steele, M., R. Morley, and W. Ermold, 2001: PHC: A global ocean hydrography with a  
 1012 high quality Arctic Ocean. *J. Climate*, **14**, 2079-2087.

1013 Still, C. J., J. A. Berry, G. J. Collatz, and R. S. DeFries, 2003: Global distribution of C3  
 1014 and C4 vegetation: Carbon cycle implications. *Global Biogeochem. Cycles*, **17**,

1015           1006, doi:10.1029/2001GB001807.

1016   Stouffer, R. J., A. J. Weaver, and M. Edy, 2004: A method for obtaining pretwentieth  
1017           century initial conditions for use in climate change studies. *Clim. Dyn.*, **23**, 327-  
1018           339.

1019   Sudo, K., M. Takahashi, J. Kurokawa, and H. Akimoto, 2002: CHASER: A global  
1020           chemical model of the troposphere 1. Model description. *J. Geophys. Res.*, **107**,  
1021           10.1029/2001JD001113.

1022   Takata, K., S. Emori, and T. Watanabe, 2003: Development of the Minimal Advanced  
1023           Treatments of Surface Interaction and RunOff (MATSIRO). *Global and Planetary*  
1024           *Change*, **38**, 209-222.

1025   Takemura, T., T. Nozawa, S. Emori, T. Y. Nakajima, and T. Nakajima, 2005:  
1026           Simulation of climate response to aerosol direct and indirect effects with aerosol  
1027           transport-radiation model. *J. Geophys. Res.*, **110**, D02202, doi:10.1029/  
1028           2004JD005029.

1029   Takemura, T., M. Egashira, K. Matsuzawa, H. Ichijo, R. O'ishi, and A. Abe-Ouchi,  
1030           2009: A simulation of the global distribution and radiative forcing of soil dust  
1031           aerosols at the Last Glacial Maximum. *Atmos. Chem. Phys.*, **9**, 3061-3073.

1032   Tally, L., 1993: Distribution and formation of North Pacific intermediate water. *J. Phys.*  
1033           *Oceanogr.*, **23**, 517-537.

1034   Thorndike, A. S., D. S. Rothrock, G. A. Maykut, and R. Colony, 1975: The thickness  
1035           distribution of sea ice. *J. Geophys. Res.*, **80**, 4501-4513.

1036   Tomita, H., and M. Satoh, 2004: A new dynamical framework of nonhydrostatic global  
1037           model using the icosahedral grid. *Fluid Dynamics Research*, **34**, 357-400.

1038   Trenberth, K. E., and D. J. Shea, 2006: Atlantic hurricanes and natural variability in  
1039           2005. *Geophys. Res. Lett.*, **33**, doi:10.1029/2006GL026894.

1040 Tsushima, Y., and Coauthors, 2006: Importance of the mixed-phase cloud distribution  
1041 in the control climate for assessing the response of clouds to carbon dioxide  
1042 increase: a multi-model study. *Clim. Dyn.*, **27**, doi:10.1007/s00382-006-0127-7.

1043 Uppala, S. M., and Coauthors, 2005: The ERA-40 re-analysis. *Quart. J. Roy. Meteor.*  
1044 *Soc.*, **131**, 2961-3012.

1045 Waliser, D. E., and Coauthors, 2009: Cloud ice: A climate model challenge with signs  
1046 and expectations of progress. *J. Geophys. Res.*, **114**, D00A21,  
1047 doi:10.1029/2008JD010015.

1048 Watanabe, M., S. Emori, M. Satoh, and H. Miura, 2009: A PDF-based hybrid  
1049 prognostic cloud scheme for general circulation models. *Clim. Dyn.*, **33**,  
1050 doi:10.1007/s00382-008-0489-0.

1051 Watanabe, M., M. Chikira, Y. Imada, and M. Kimoto, 2010: Convective control of  
1052 ENSO simulated in MIROC. *J. Climate*, submitted.

1053 Watanabe, S., H. Miura, M. Sekiguchi, T. Nagashima, K. Sudo, S. Emori, and M.  
1054 Kawamiya, 2008: Development of an atmospheric general circulation model for  
1055 integrated Earth system modeling on the Earth simulator. *J. Earth Simulator*, **9**, 28-  
1056 35.

1057 Wheeler, M., and G. N. Kiladis, 1999: Convectively coupled equatorial waves: Analysis  
1058 of clouds and temperature in the wavenumber-frequency domain. *J. Atmos. Sci.*, **56**,  
1059 374-399.

1060 Williams, P. D., 2009: A proposed modification to the Robert–Asselin time filter. *Mon.*  
1061 *Wea. Rev.*, **137**, 2538-2546.

1062 Wilson, D. R., and S. P. Ballard, 1999: A microphysically based precipitation scheme  
1063 for the UK Meteorological Office unified model. *Quart. J. Roy. Met. Soc.*, **125**,  
1064 1607-1636.

1065 Xie, P., and P. A. Arkin, 1997: Global precipitation: a 17-year monthly analysis based  
 1066 on gauge observations, satellite estimates, and numerical model outputs. *Bull.*  
 1067 *Amer. Meteor. Soc.*, **78**, 2539-2558.

1068 Xu, K.-M., 1993: Cumulus ensemble simulation, the representation of cumulus  
 1069 convection in numerical models. *Meteor. Monogr.*, **24**, 221-235.

1070 Yamazaki, D., T. Oki, and S. Kanae, 2009: Deriving a global river network map and its  
 1071 sub-grid topographic characteristics from a fine-resolution flow direction map.  
 1072 *Hydrol. Earth Syst. Sci.*, **13**, 2241-2251.

1073 Yang, Z.-L., R. E. Dickinson, A. Robock, and K. Y. Vinnikov, 1997: Validation of the  
 1074 snow submodel of the biosphere-atmosphere transfer scheme with Russian snow  
 1075 cover and meteorological observational data. *J. Climate*, **10**, 353-373.

1076 Yasuda, I., 1997: The origin of the North Pacific Intermediate Water. *J. Geophys. Res.*,  
 1077 **102**, 893-909.

1078 Yokohata, T., M. J. Webb, M. Collins, K. Williams, M. Yoshimori, J. Hargreaves, and J.  
 1079 D. Annan, 2010: Structural similarities and differences in climate responses to  
 1080 CO<sub>2</sub> increase between two perturbed physics ensembles. *J. Climate*, in press.

1081 Yoshida, R., H. Okamoto, Y. Hagihara, and H. Ishimoto, 2010: Global analysis of cloud  
 1082 phase and ice crystal orientation from CALIPSO data using attenuated  
 1083 backscattering and depolarization ratio. *J. Geophys. Res.*, in press.

1084 Zhang, Y.-C., W. B. Rossow, A. A. Lacis, V. Oinas, and M. I. Mishchenko, 2004:  
 1085 Calculation of radiative fluxes from the surface to top of atmosphere based on  
 1086 ISCCP and other global data sets: Refinements of the radiative transfer model and  
 1087 the input data. *J. Geophys. Res.*, **109**, D19105, doi:10.1029/2003JD004457.

1088  
 1089

1090 TABLE AND FIGURE CAPTIONS

1091

1092 Table 1 Global mean radiative and energy budgets from observational estimates,  
 1093 MIROC3, and MIROC5. Radiative budgets given in  $\text{W m}^{-2}$  are the values at  
 1094 TOA. References for the observational estimates are shown at the bottom. All  
 1095 the quantities are the annual averages.

1096 Fig. 1 Time series of global mean SST (thick black), VAT700 (thin black), and VAT  
 1097 (gray) for control integration of MIROC5.

1098 Fig. 2 (a) Annual mean climatology of the net LW in MIROC5, and biases in the  
 1099 annual mean LW climatology in (b) MIROC3med and (c) MIROC5. (d)–(f) As  
 1100 in (a)–(c) but for the net incoming SW. The unit is  $\text{W m}^{-2}$ .

1101 Fig. 3 Annual mean climatology of SST from (a) observations and (b) MIROC5. The  
 1102 unit is  $^{\circ}\text{C}$  and the contour interval is  $1^{\circ}\text{C}$  (drawn only above  $26^{\circ}\text{C}$ ).

1103 Fig. 4 Biases in the annual mean climatology of (a) SST and (b) SSS in MIROC3med.  
 1104 (c)–(d) As in (a)–(b) but for MIROC5. The units are  $^{\circ}\text{C}$  and psu, respectively.

1105 Fig. 5 Annual mean climatology of precipitation from (a) CMAP and (b) MIROC5.  
 1106 The unit is  $\text{mm d}^{-1}$ .

1107 Fig. 6 Biases relative to CMAP data in annual mean precipitation in (a) MIROC3med,  
 1108 (b) MIROC3hi, and (c) MIROC5. The unit is  $\text{mm d}^{-1}$ .

1109 Fig. 7 Climatological precipitation and 850 hPa winds in JJA from (a) TRMM PR and  
 1110 ERA40, (b) MIROC3med, (c) MIROC3hi, and (d) MIROC5. The units are  $\text{mm}$   
 1111  $\text{mo}^{-1}$  and  $\text{m s}^{-1}$ .

1112 Fig. 8 Biases in annual and zonal mean climatology of the zonal wind in (a)  
 1113 MIROC3med and (b) MIROC5. The unit is  $\text{m s}^{-1}$  and the model climatology is

1114 shown by contours. (c)–(d) As in (a)–(b) but for temperature (K). (e)–(f) As in  
1115 (a)–(b) but for water vapor specific humidity ( $\text{g kg}^{-1}$ ).

1116 Fig. 9 Annual mean climatology along equator of (a) zonal wind stress ( $\text{N m}^{-2}$ ) and (b)  
1117 SST ( $^{\circ}\text{C}$ ) from observations and models. (c) Annual mean climatology along  
1118 equator of observed ocean temperature (shading,  $^{\circ}\text{C}$ ) and ocean zonal current  
1119 (contour interval:  $10 \text{ cm s}^{-1}$ ) estimated by SODA analysis. (d)–(e) As in (c) but  
1120 for the MIROC3med and MIROC5, respectively.

1121 Fig. 10 Climatological Arctic sea ice concentration in (a) JFM and (b) JAS derived  
1122 from observations. (c)–(d) As in (a)–(b) but for the Antarctic sea ice. (e)–(h) As  
1123 in (a)–(d) but for MIROC5.

1124 Fig. 11 (a) Annual mean climatology of Atlantic meridional overturning circulation  
1125 (contours, Sv) and bias of zonal mean temperature in Atlantic Ocean in  
1126 MIROC3med (shading, K). (b) Time series of maximum (black) and equatorial  
1127 (red) transport of the Atlantic meridional overturning circulation in  
1128 MIROC3med. (c)–(d) As in (a)–(b) but for MIROC5.

1129 Fig. 12 Zonal wavenumber-frequency power spectra of symmetric component of OLR  
1130 divided by background power, obtained from (a) NOAA satellite, (b)  
1131 MIROC3med, (c) MIROC3hi, and (d) MIROC5, based on 30-y daily data.  
1132 Dispersion curves of equatorial waves for the three equivalent depths of 12, 25,  
1133 and 50 m are indicated by red lines. Signals corresponding to the westward and  
1134 eastward inertio-gravity waves (WIG and EIG), equatorial Rossby waves (ER),  
1135 equatorial Kelvin waves, and MJO are labeled in (a).

1136 Fig. 13 Time series of Niño 3 SST anomaly: (a) observations, (b) MIROC3med, (c)  
1137 MIROC3hi, and (d) MIROC5. The standard deviation in K is indicated in each

1138 panel.

1139 Fig. 14 Monthly anomalies in observed (a) SST (K), (b) precipitation (mm d<sup>-1</sup>), and (c)  
1140 500 hPa height (m) regressed upon the Niño 3 SST time series. The contour  
1141 intervals are 0.2 K, 0.5 mm d<sup>-1</sup>, and 5 m (zero contours omitted), respectively.  
1142 (d)–(f) As in (a)–(c) but for MIROC5. The shading indicates the correlation  
1143 coefficient.

1144 Fig. 15 Scatter plot of Niño 4  $\tau_x$  anomaly against Niño 3 SST anomaly in (a)  
1145 MIROC3med and (b) MIROC5. The value of the regression slope that defines  $\mu$   
1146 ( $10^{-3} \text{ N m}^{-2} \text{ K}^{-1}$ ) is denoted at the bottom-right corner.

1147 Fig. 16 (a)–(b) Annual mean cloud ice mixing ratio at 215 hPa derived from satellite  
1148 estimates (adopted from Fig. 16 of Waliser et al. 2009). The unit is  $10^{-6} \text{ kg m}^{-3}$ .  
1149 (c)–(d) As in (a)–(b) but for MIROC3med and MIROC5, respectively.

1150 Fig. 17 Latitudinal distribution of annual mean cloud liquid fraction,  $F_{\text{liq}}$ , as a function  
1151 of temperature: (a) 2006–2007 mean of the CALIPSO data (Yoshida et al. 2009,  
1152 updated by H Okamoto) and (b) climatology in MIROC5.

1153 Fig. 18 Gregory plots obtained from abrupt CO<sub>2</sub>x4 experiment in (a) MIROC3med and  
1154 (b) MIROC5 (see text for the experiment). The intersection between the net  
1155 radiative flux at TOA (black line) and the horizontal axis (divided by 2)  
1156 indicates the equilibrium climate sensitivity.

1157 Fig. 19 Changes in annual mean low cloud fraction (%) obtained from control run and  
1158 abrupt CO<sub>2</sub>x4 experiment in (a) MIROC3med and (b) MIROC5.

1159

1160



1161

1162

1163 Table 1. Global mean radiative and energy budgets from observational estimates,

1164 MIROC3, and MIROC5. Radiative budgets given in  $\text{W m}^{-2}$  are the values at TOA.

1165 References for the observational estimates are shown at the bottom. All the quantities

1166 are the annual averages.

1167

Parameter	Observed	MIROC3med	MIROC3hi	MIROC5
Incoming solar	341.5 <sup>*</sup> /341.8 <sup>+</sup>	341.6	341.5	341.5
Net SW (all sky)	235.8 <sup>*</sup> /240.5 <sup>+</sup>	235.7	240.0	237.6
Net LW (all sky)	236.3 <sup>*</sup> /239.6 <sup>+</sup>	234.8	239.4	236.5
Net (all sky)	0.5 <sup>*</sup> /0.85 <sup>+</sup>	-0.9	-0.6	-1.1
SW CRF	-51.0 <sup>*</sup> /-46.6 <sup>+</sup>	-53.8	-48.7	-53.8
LW CRF	26.5 <sup>*</sup> /29.5 <sup>+</sup>	27.6	27.0	26.3
Net CRF	-24.5 <sup>*</sup> /-17.1 <sup>+</sup>	-26.2	-21.7	-27.5
2m Temperature (°C)	14.0 <sup>@</sup> /14.5 <sup>##</sup>	13.4	13.9	14.5
SST (°C)	18.2 <sup>**</sup>	17.4	17.8	17.9
Precipitation (mm d <sup>-1</sup> )	2.61 <sup>#</sup>	2.72	2.96	3.2
Evaporation (mm d <sup>-1</sup> )	2.89 <sup>&amp;</sup>	2.72	2.96	3.2
P-E (mm d <sup>-1</sup> )	-0.28	0.0	0.0	0.0
Cloud cover (%)	60 <sup>++</sup>	51.9	51.8	56.3

1168 \* ISCCP FD dataset (Zhang et al. 2004)

1169 + Adjusted CERES (Loeb et al. 2009)

1170 # CMAP 1979-2007 mean (Xie and Arkin 1997)

1171 &amp; OMIP (Roeske 2001)

1172 @ CRU 1961-1990 mean (Jones et al. 2001)

1173 \*\* Ishii et al. (2006), 1945-2006 mean

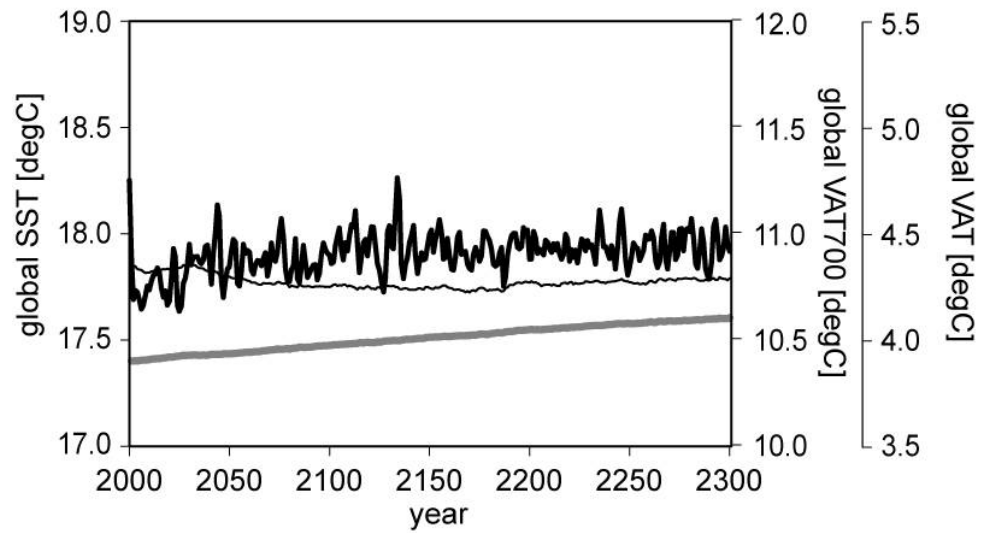
1174 ++ Kiehl and Trenberth (1997)

1175 ## ERA40 (Uppala et al. 2005)

1176

1177

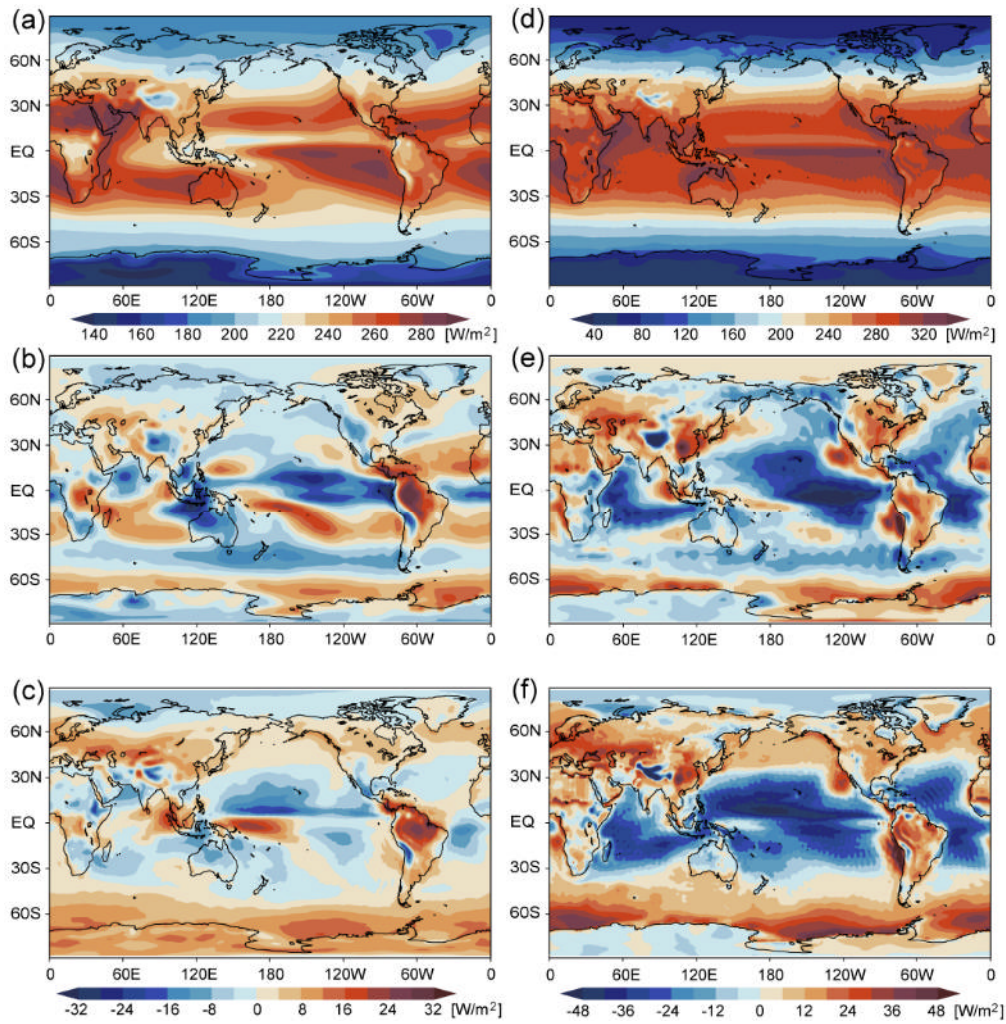
1178  
1179  
1180  
1181  
1182



1183

1184 Fig. 1 Time series of global mean SST (thick black), VAT700 (thin black), and VAT  
1185 (gray) for control integration of MIROC5.

1186  
1187  
1188  
1189  
1190  
1191  
1192



1193

1194

1195

1196 Fig. 2 (a) Annual mean climatology of the net LW in MIROC5, and biases in the  
 1197 annual mean LW climatology in (b) MIROC3med and (c) MIROC5. (d)–(f) As in (a)–  
 1198 (c) but for the net incoming SW. The unit is  $\text{W m}^{-2}$ .

1199

1200

1201

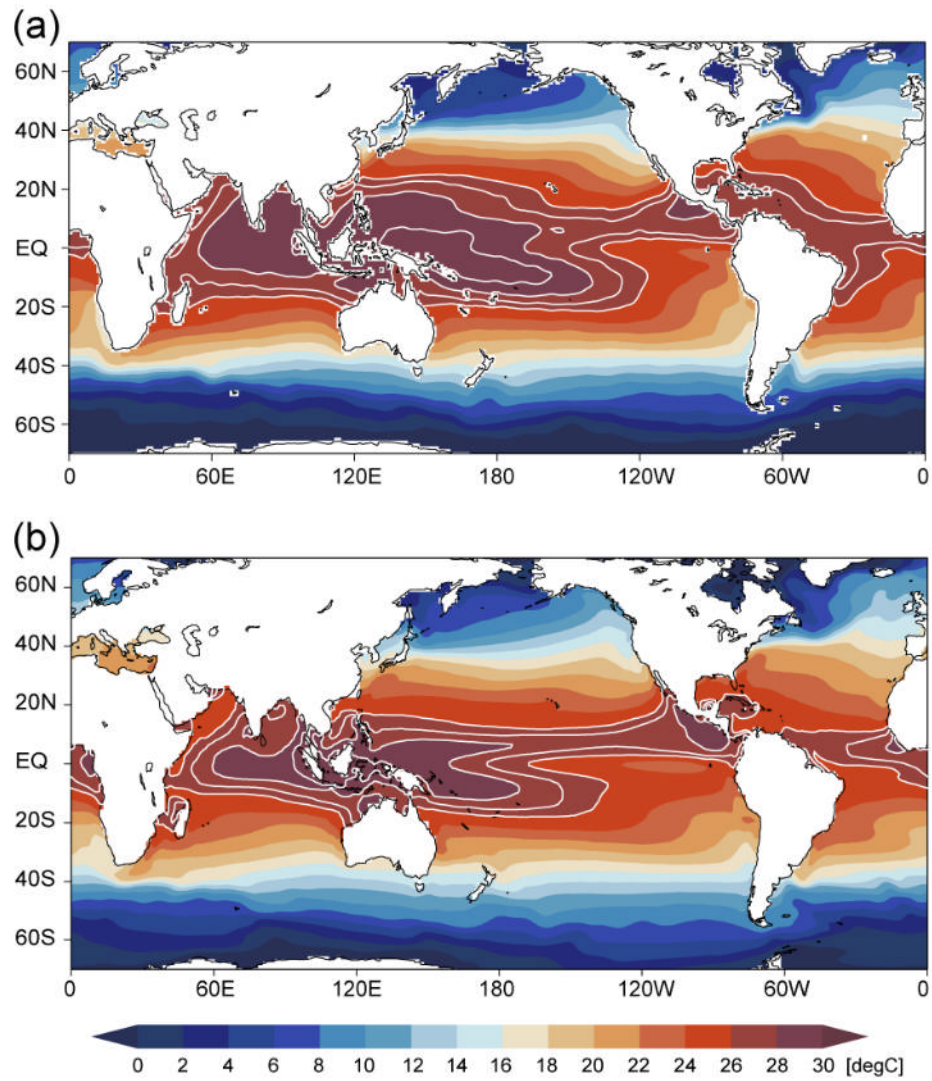
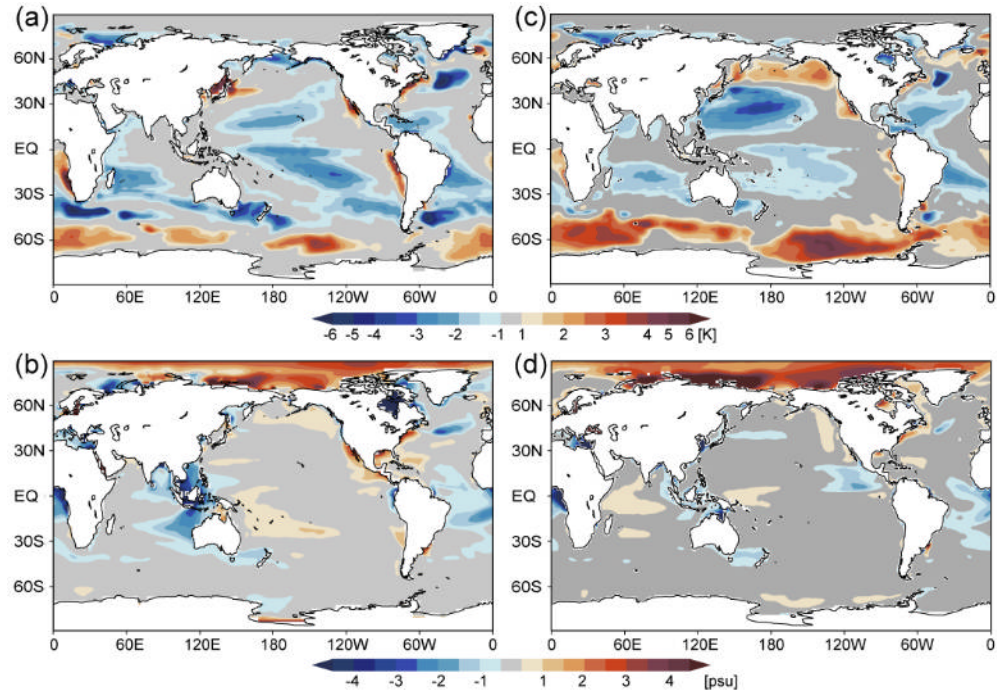


Fig. 3 Annual mean climatology of SST from (a) observations and (b) MIROC5. The unit is  $^{\circ}\text{C}$  and the contour interval is  $1^{\circ}\text{C}$  (drawn only above  $26^{\circ}\text{C}$ ).

1226

1227



1228

1229

1230

1231 Fig. 4 Biases in the annual mean climatology of (a) SST and (b) SSS in MIROC3med.

1232 (c)–(d) As in (a)–(b) but for MIROC5. The units are °C and psu, respectively.

1233

1234

1235

1236

1237

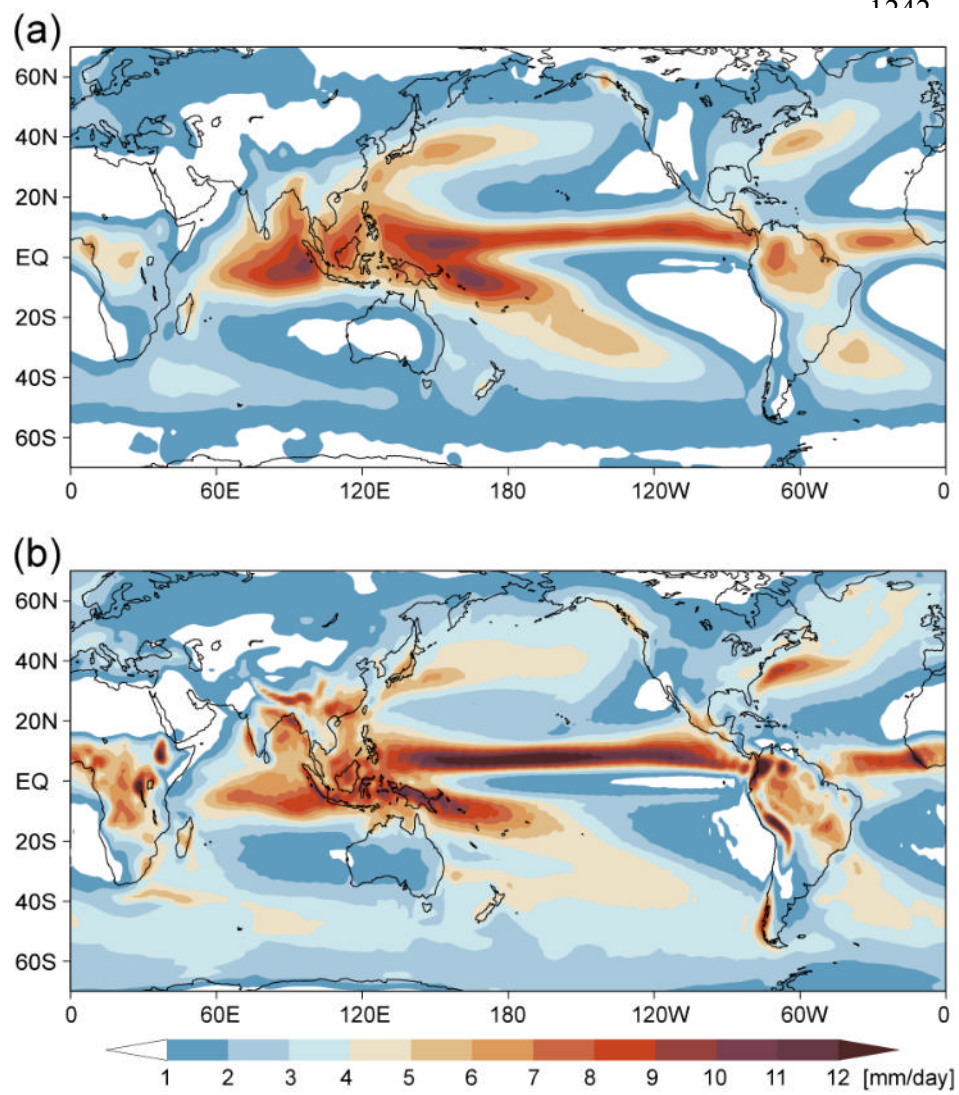
1238

1239



1240

1241



1258

1259

1260 Fig. 5 Annual mean climatology of precipitation from (a) CMAP and (b) MIROC5.

1261 The unit is  $\text{mm d}^{-1}$ .

1262

1263

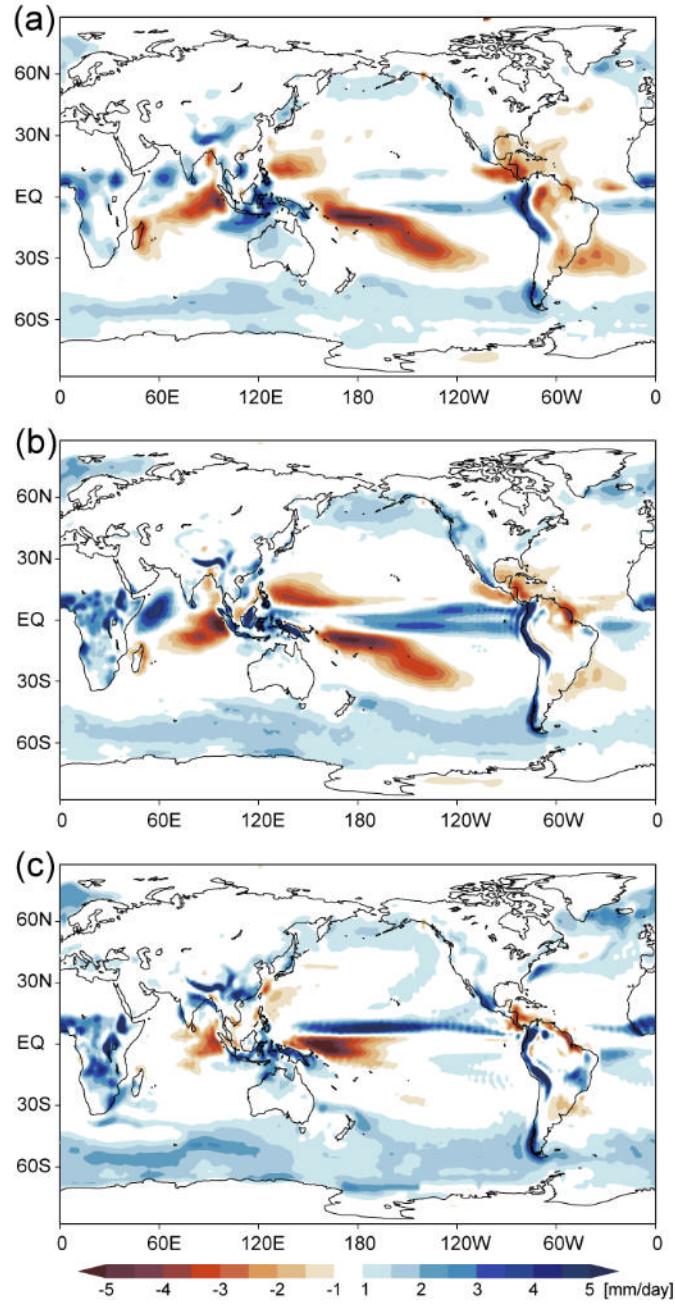
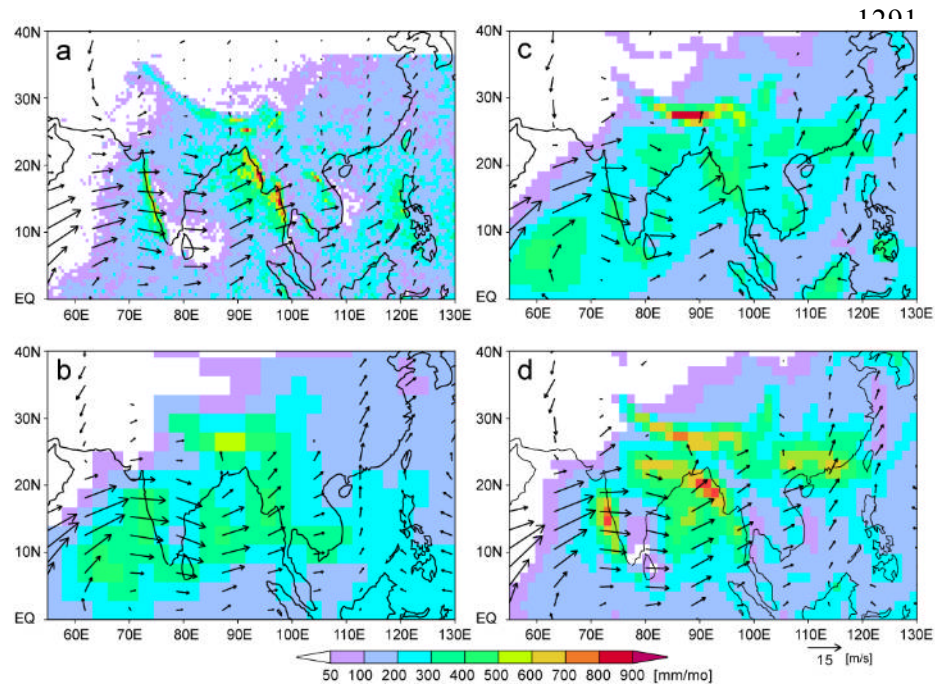


Fig. 6 Biases relative to CMAP data in annual mean precipitation in (a) MIROC3med, (b) MIROC3hi, and (c) MIROC5. The unit is  $\text{mm d}^{-1}$ .

1288

1289

1290



1301

1302

1303 Fig. 7 Climatological precipitation and 850 hPa winds in JJA from (a) TRMM PR and  
1304 ERA40, (b) MIROC3med, (c) MIROC3hi, and (d) MIROC5. The units are  $\text{mm mo}^{-1}$   
1305 and  $\text{m s}^{-1}$ .

1306

1307

1308

1309

1310

1311

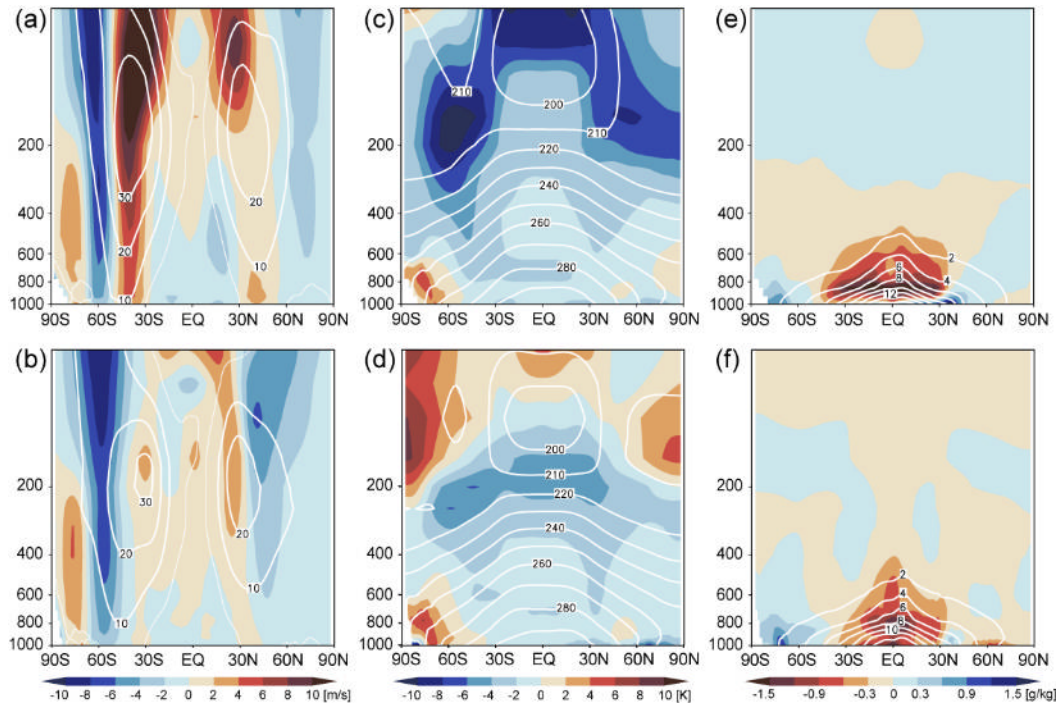


1312

1313

1314

1315



1316

1317

1318 Fig. 8 Biases in annual and zonal mean climatology of the zonal wind in (a)  
 1319 MIROC3med and (b) MIROC5. The unit is  $\text{m s}^{-1}$  and the model climatology is shown  
 1320 by contours. (c)–(d) As in (a)–(b) but for temperature (K). (e)–(f) As in (a)–(b) but for  
 1321 water vapor specific humidity ( $\text{g kg}^{-1}$ ).

1322

1323

1324

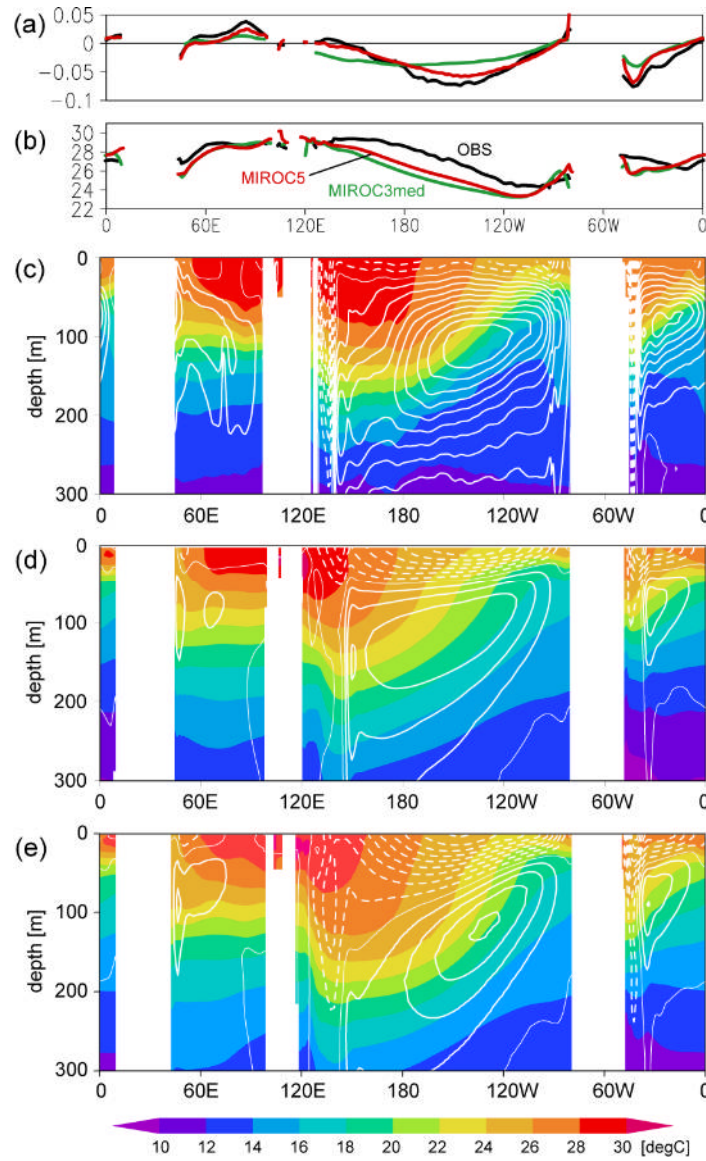


Fig. 9 Annual mean climatology along equator of (a) zonal wind stress ( $\text{N m}^{-2}$ ) and (b) SST ( $^{\circ}\text{C}$ ) from observations and models. (c) Annual mean climatology along equator of observed ocean temperature (shading,  $^{\circ}\text{C}$ ) and ocean zonal current (contour interval:  $10 \text{ cm s}^{-1}$ ) estimated by SODA analysis. (d)–(e) As in (c) but for the MIROC3med and MIROC5, respectively.

1349

1350

1351

1352

1353

1354

1355

1356

1357

1358

1359

1360

1361

1362

1363

1364

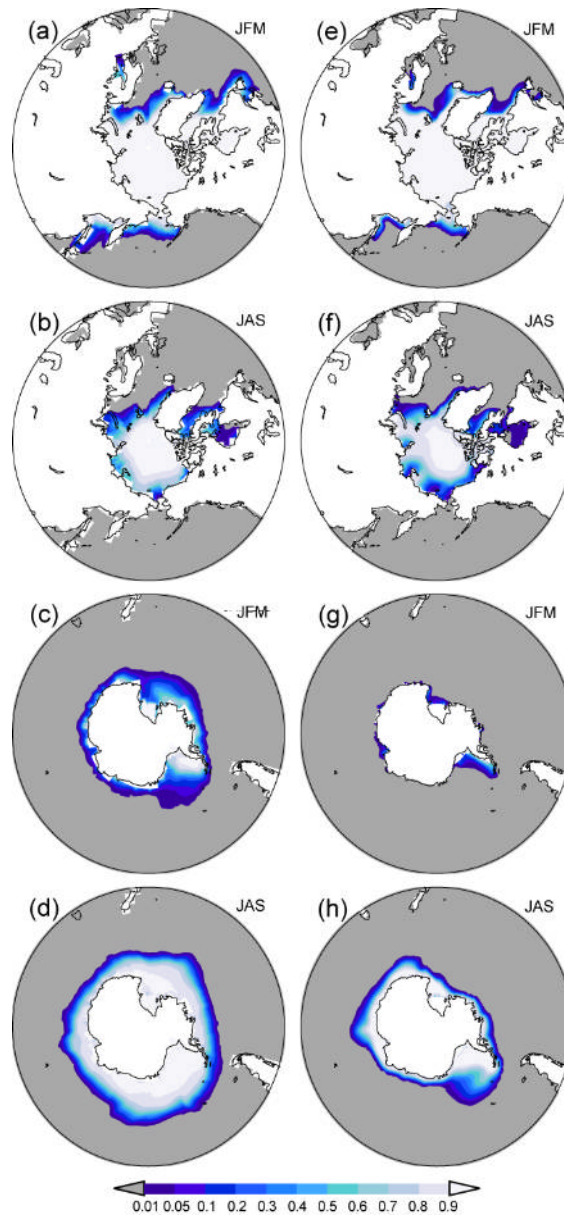
1365

1366

1367

1368

1369



1370 Fig. 10 Climatological Arctic sea ice concentration in (a) JFM and (b) JAS derived

1371 from observations. (c)–(d) As in (a)–(b) but for the Antarctic sea ice. (e)–(h) As in (a)–

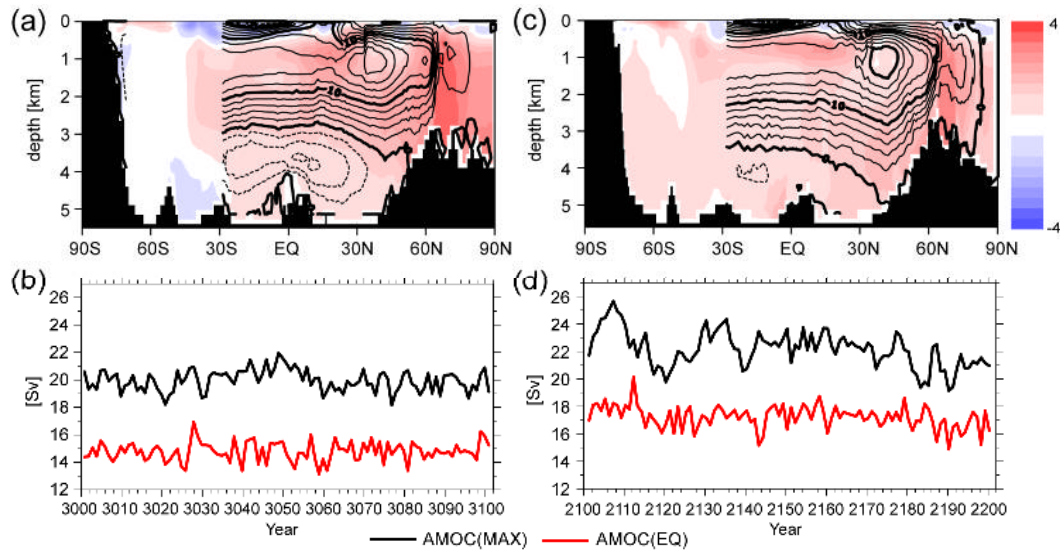
1372 (d) but for MIROC5.

1373

1374

1375

1376



1377

1378

1379

1380 Fig. 11 (a) Annual mean climatology of Atlantic meridional overturning circulation

1381 (contours, Sv) and bias of zonal mean temperature in Atlantic Ocean in MIROC3med

1382 (shading, K). (b) Time series of maximum (black) and equatorial (red) transport of the

1383 Atlantic meridional overturning circulation in MIROC3med. (c)–(d) As in (a)–(b) but

1384 for MIROC5.

1385

1386

1387

1388

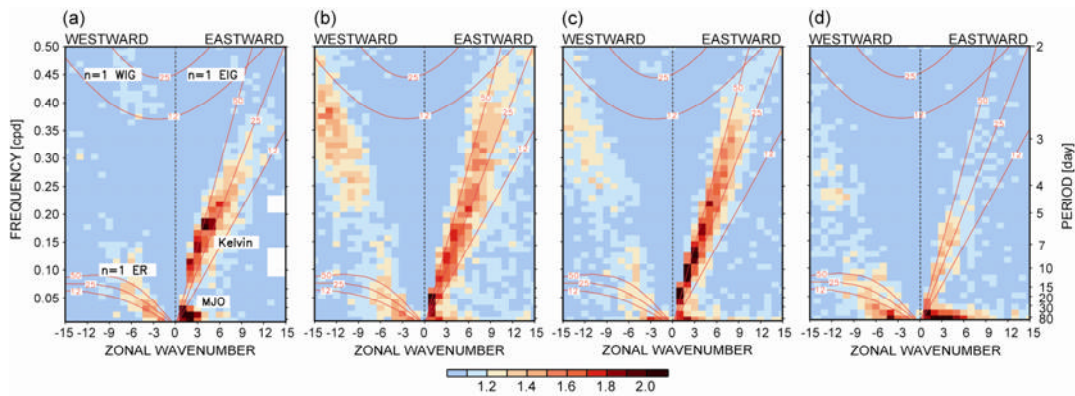
1389

1390

1391

1392

1393



1394

1395

1396 Fig. 12 Zonal wavenumber-frequency power spectra of symmetric component of OLR

1397 divided by background power, obtained from (a) NOAA satellite, (b) MIROC3med, (c)

1398 MIROC3hi, and (d) MIROC5, based on 30-y daily data. The dispersion curves of

1399 equatorial waves for the three equivalent depths of 12, 25, and 50 m are indicated by red

1400 lines. Signals corresponding to the westward and eastward inertio-gravity waves (WIG

1401 and EIG), equatorial Rossby waves (ER), equatorial Kelvin waves, and MJO are labeled

1402 in (a).

1403

1404

1405

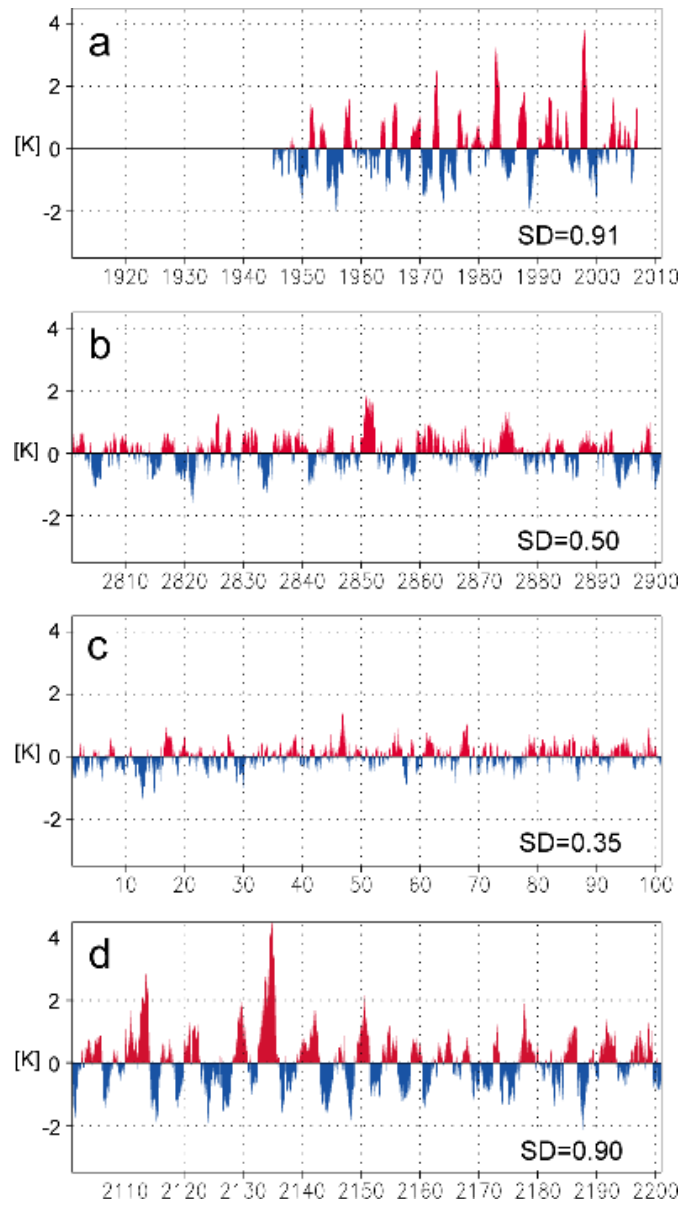


Fig. 13 Time series of Niño 3 SST anomaly: (a) observations, (b) MIROC3med, (c) MIROC3hi, and (d) MIROC5. The standard deviation in K is indicated in each panel.

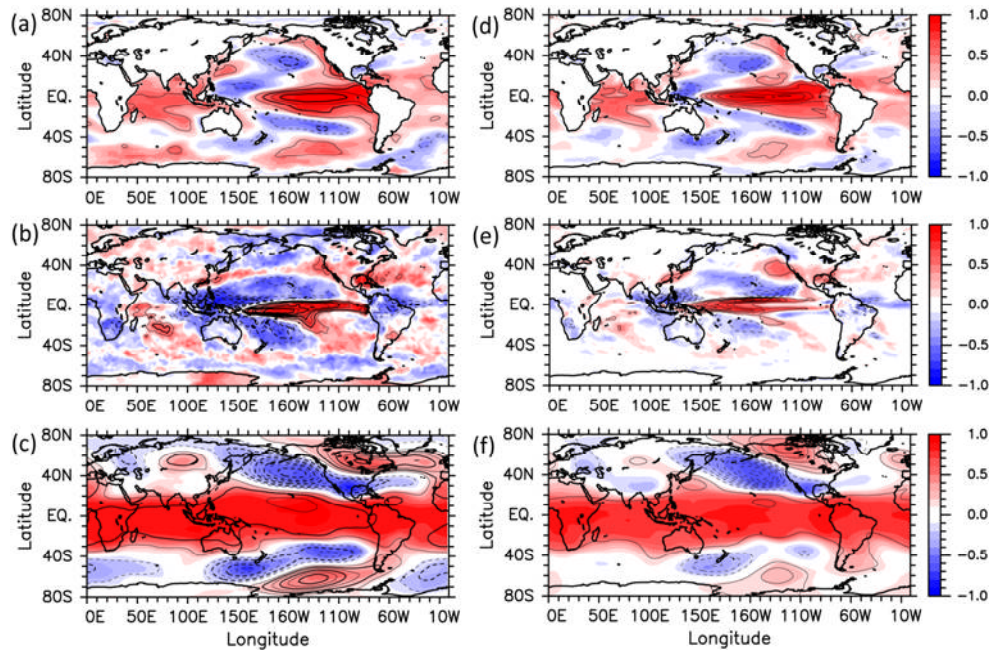


1430

1431

1432

1433



1434

1435

1436 Fig. 14 Monthly anomalies in observed (a) SST (K), (b) precipitation (mm d<sup>-1</sup>), and (c)  
 1437 500 hPa height (m) regressed upon the Niño 3 SST time series. The contour intervals  
 1438 are 0.2 K, 0.5 mm d<sup>-1</sup>, and 5 m (zero contours omitted), respectively. (d)–(f) As in (a)–  
 1439 (c) but for MIROC5. The shading indicates the correlation coefficient.

1440

1441

1442

1443

1444

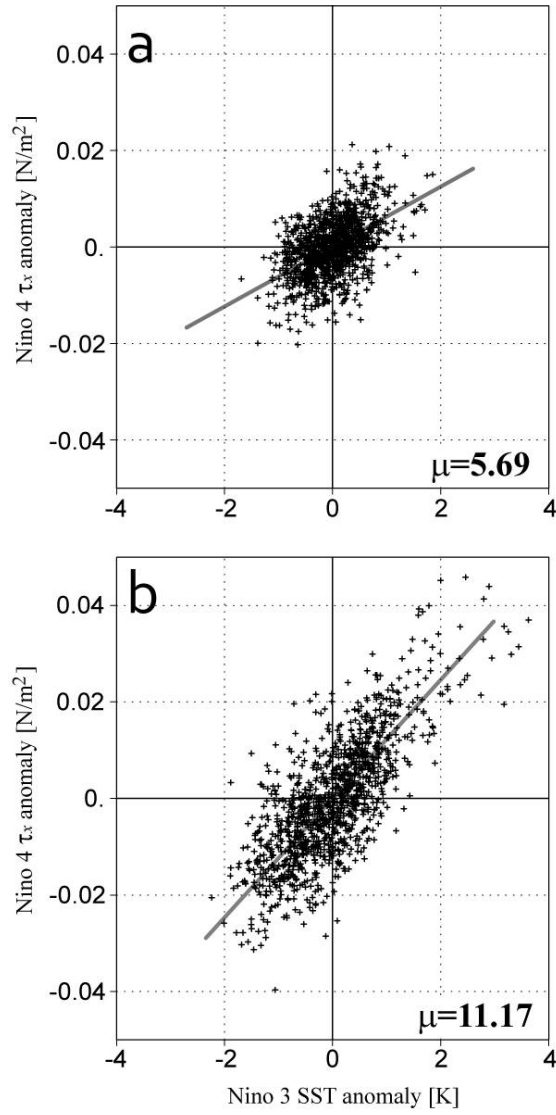


Fig. 15 Scatter plot of Niño 4  $\tau_x$  anomaly against Niño 3 SST anomaly in (a) MIROC3med and (b) MIROC5. The value of the regression slope that defines  $\mu$  ( $10^{-3}$  N m<sup>-2</sup> K<sup>-1</sup>) is denoted at the bottom-right corner.

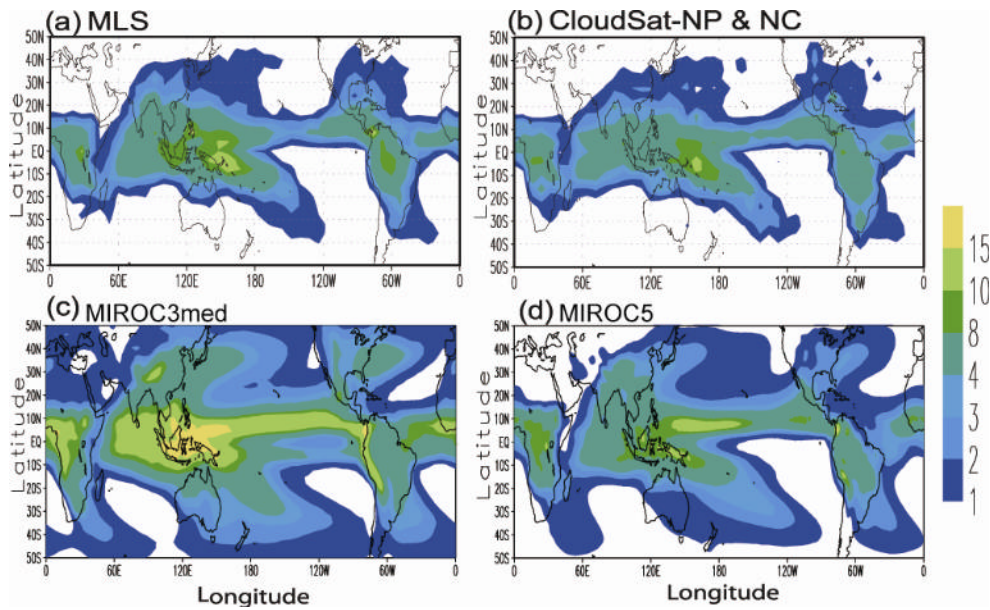


1469

1470

1471

1472



1473

1474

1475 Fig. 16 (a)–(b) Annual mean cloud ice mixing ratio at 215 hPa derived from satellite  
1476 estimates (adopted from Fig. 16 of Waliser et al. 2009). The unit is  $10^{-6} \text{ kg m}^{-3}$ . (c)–(d)  
1477 As in (a)–(b) but for MIROC3med and MIROC5, respectively.

1478

1479

1480

1481

1482

1483

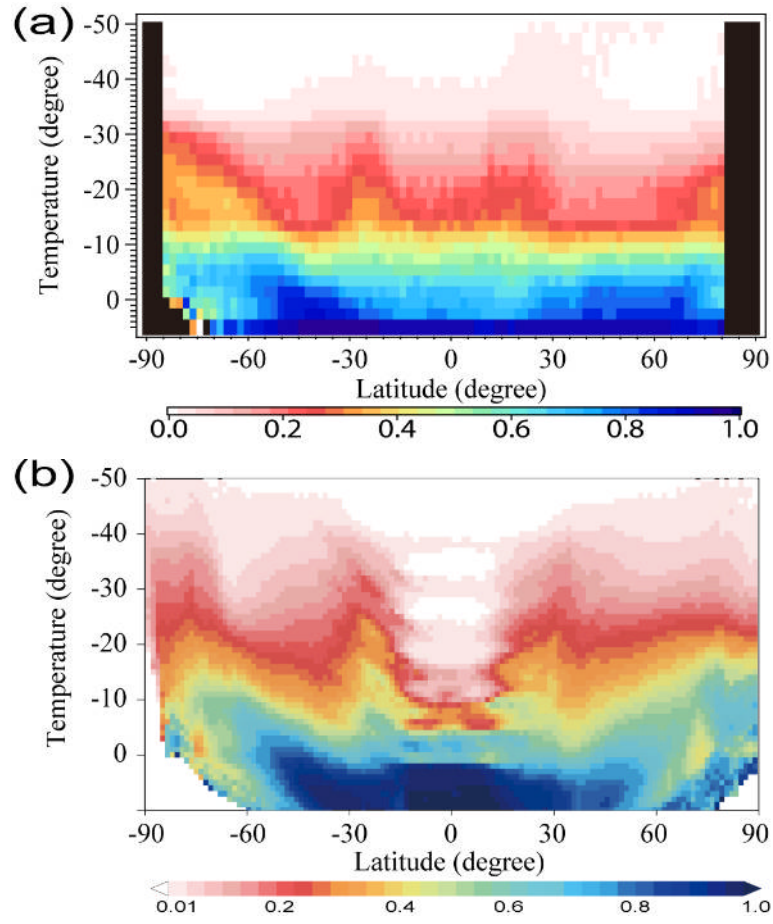


Fig. 17 Latitudinal distribution of annual mean cloud liquid fraction,  $F_{liq}$ , as a function of temperature: (a) 2006–2007 mean of the CALIPSO data (Yoshida et al. 2009, updated by H Okamoto) and (b) climatology in MIROC5.

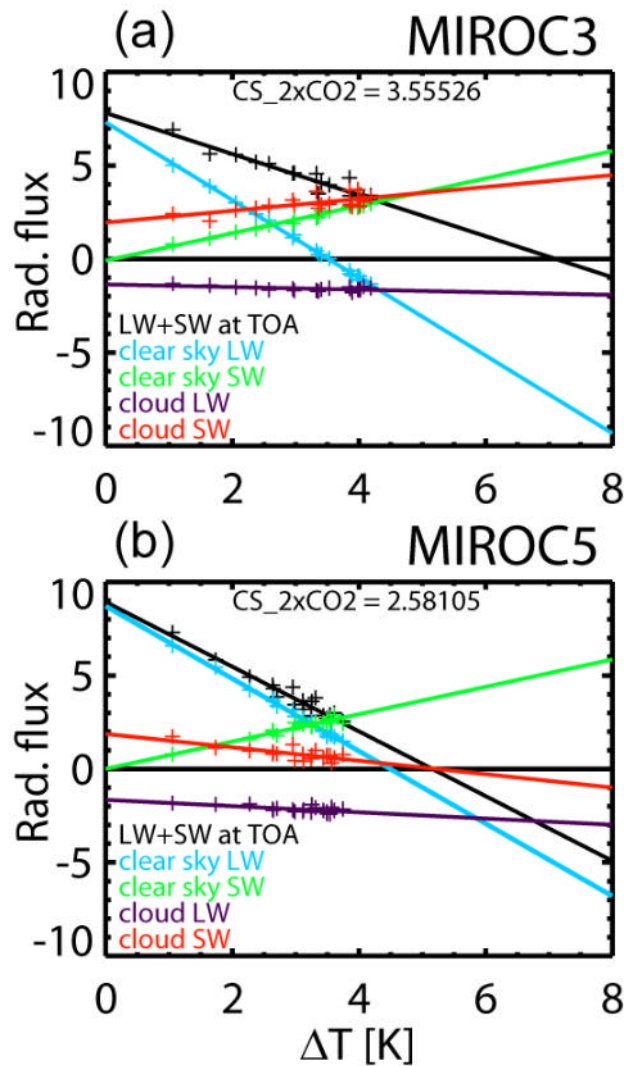


Fig. 18 Gregory plots obtained from abrupt  $CO_2 \times 4$  experiment in (a) MIROC3med and (b) MIROC5 (see text for the experiment). The intersection between the net radiative flux at TOA (black line) and the horizontal axis (divided by 2) indicates the equilibrium climate sensitivity.

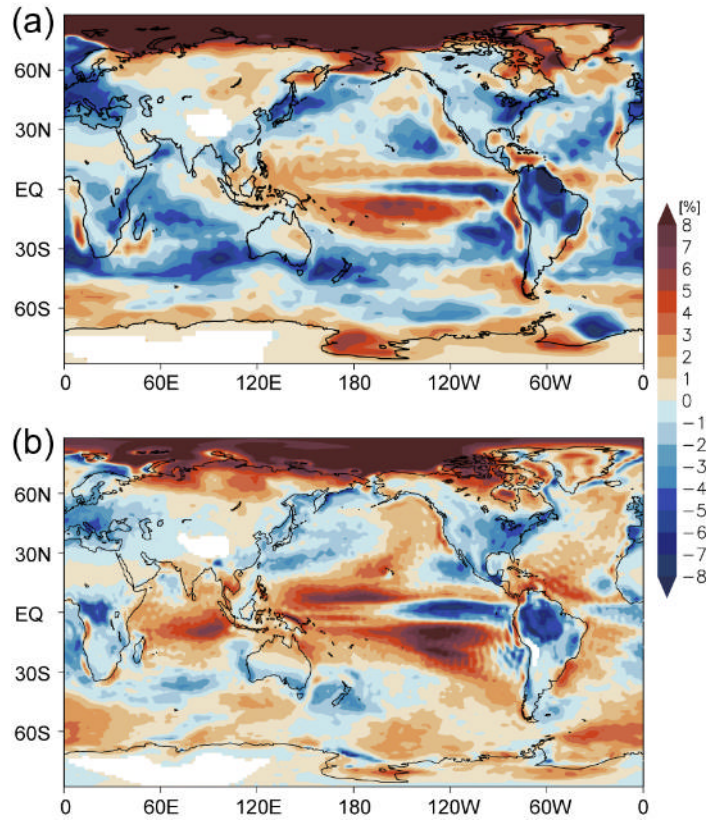


Fig. 19 Changes in annual mean low cloud fraction (%) obtained from control run and abrupt CO<sub>2</sub>x4 experiment in (a) MIROC3med and (b) MIROC5.